




2022

The Vagabond Flourine Atom Revisited: Dissociative Photoionization of Tri- and Pentafluoropropene

Jessica K. De La Cruz
University of the Pacific

Follow this and additional works at: https://scholarlycommons.pacific.edu/uop_etds

 Part of the [Medicinal and Pharmaceutical Chemistry Commons](#), and the [Medicinal-Pharmaceutical Chemistry Commons](#)

Recommended Citation

De La Cruz, Jessica K.. (2022). *The Vagabond Flourine Atom Revisited: Dissociative Photoionization of Tri- and Pentafluoropropene*. University of the Pacific, Thesis. https://scholarlycommons.pacific.edu/uop_etds/3785

This Thesis is brought to you for free and open access by the Graduate School at Scholarly Commons. It has been accepted for inclusion in University of the Pacific Theses and Dissertations by an authorized administrator of Scholarly Commons. For more information, please contact m gibney@pacific.edu.

THE VAGABOND FLOURINE ATOM REVISITED: DISSOCIATIVE PHOTOIONIZATION
OF TRI- AND PENTAFLUOROPROPENE

By

Jessica Kaelyn De La Cruz

A Thesis Submitted to the

Graduate School

In Partial Fulfillment of the

Requirements for the Degree of

MASTER OF SCIENCE

Thomas J. Long School of Pharmacy and Health Sciences
Pharmaceutical and Chemical Sciences

University of the Pacific
Stockton, California

2022

THE VAGABOND FLOURINE ATOM REVISITED: DISSOCIATIVE PHOTOIONIZATION
OF TRI- AND PENTAFLUOROPROPENE

By

Jessica Kaelyn De La Cruz

APPROVED BY:

Thesis Advisor: Bálint Sztáray, Ph.D.

Committee Member: Michael McCallum, Ph.D.

Committee Member: Qinliang Zhao, Ph.D.

Department Co-Chair: Jianhua Ren, Ph.D.

Department Co-Chair: Jerry Tsai, Ph.D.

Dean of College of the Pacific: Rena Fraden, Ph.D.

THE VAGABOND FLOURINE ATOM REVISITED: DISSOCIATIVE PHOTOIONIZATION
OF TRI- AND PENTAFLUOROPROPENE

Copyright 2022

By

Jessica Kaelyn De La Cruz

DEDICATION

In memory of my mother, Lacinda De La Cruz. You were an incredibly strong woman and I strive to be as kind, generous, compassionate, and all around as amazing of a human being as you were.

ACKNOWLEDGEMENTS

First and foremost, I am thankful for my advisor, Dr. Bálint Sztáray for his guidance through both my undergraduate and graduate degrees at University of the Pacific. During my graduate studies he presented me with the opportunity to work at two world renown research facilities: SOLEIL synchrotron in France and the Swiss Light Source in Switzerland. I would also like to express my gratitude to everyone who has been a part of the Sztáray research group throughout my studies (Dr. Amelia Ray, Dr. Péter Weidner, Dr. Krisztián Torma, Dr. Krisztina Voronova, and Dr. Kyle Covert). They have all made long research days enjoyable with the lunch dates pre-COVID and Zoom/WebEx chats during COVID. Thank you all for all the knowledge you have shared with me.

I would not have achieved this accomplishment without my family and all my loved ones. Although none of you ever understood my studies, I knew you were all supportive of me. I am extremely grateful for the countless texts, calls, and facetimes to give me well needed breaks.

I also appreciate everyone else within the Chemistry Department, both past and present, who has made this this department feel like a home. A special thank you to Dr. Michael McCallum and Dr. Qinliang Zhao for serving on my thesis committee. My years at University of the Pacific have been extremely enjoyable and it is bittersweet that it has now come to an end.

THE VAGABOND FLOURINE ATOM REVISITED: DISSOCIATIVE PHOTOIONIZATION OF TRI- AND PENTAFLUOROPROPENE

Abstract

By Jessica Kaelyn De La Cruz

University of the Pacific
2022

Photoelectron Photoion Coincidence (PEPICO) Spectroscopy studies on two unsaturated hydrofluorocarbons (HFCs), also known as hydrofluoroolefines (HFOs), are presented here. Previously, the Sztáray group has studied the dissociation of *trans*-1,3,3,3-tetrafluoroprop-1-ene (ElixClean), which is a fourth-generation refrigerant and propellant and has lower global warming potential than its precursors.¹ My study is an extension of the ElixClean study as it aims to explore how the different number of fluorine atoms impact the dissociation reactions of these molecules. Both 3,3,3-trifluoropropene (TFP) and *cis*-1,2,3,3,3-pentafluoropropene (PFP) are also utilized as propellants and refrigerants.^{2,3}

Measurements were carried out with remote access to the CRF-PEPICO (combustion reactions followed by photoelectron photoion coincidence spectroscopy) endstation of the vacuum-ultraviolet (VUV) beamline at the Swiss Light Source (SLS).^{4,5} Gas phase samples were intersected with tunable vacuum ultraviolet synchrotron light to create photoions and photoelectrons which are then detected in coincidence. Breakdown diagrams were then obtained by integrating the photoelectron-photoion coincidence signal for times of flight corresponding the precursor and fragment ions and plotting their fractional abundances at each photon energy. Analysis of these dissociation mechanisms was aided by *ab initio* calculations.

Dissociative photoionization of TFP was studied over the photon energy range of 11.8–16.0 eV. Besides the molecular ion (m/z 96), there were four main fragment ions detected: m/z 95 (H-loss), 77 (F-loss), 46 (CF₂-loss), 27 (CF₃-loss). The experimental data for the dissociative photoionization of PFP was taken over the photon energy range of 12.0–16.5 eV and indicated the formation of m/z 113 (F-loss), m/z 82 (CF₂-loss), m/z 69 (C₂HF₂-loss), and m/z 51 (C₂F₃-loss), but an H-loss is not detected.

Quantum-chemical calculations at the B3LYP level were used to explore the potential energy surface and identify the most likely structures that play a role in the dissociative photoionization processes of these fluorinated propenes. The energies of the most relevant stationary points were refined utilizing G4 composite method. The dissociation/isomerization pathways of energy-selected TFP and PFP ions will be explored, and I will discuss the most likely mechanisms that lead to the lowest-energy products.

TABLE OF CONTENTS

List of Tables	9
List of Figures	10
List of Abbreviations	12
Chapter 1: Introduction	14
Chapter 2: Theory and Techniques	16
2.1 Photoelectron Photoion Coincidence Spectroscopy (PEPICO)	16
2.1.1 The Photoionization Process	16
2.1.2 Electron Detection in PEPICO and the “Hot Electron” Problem	20
2.1.3 Ion Detection in PEPICO	22
2.1.4 Coincidence Detection in Threshold PEPICO	22
2.1.5 What Can TPEPICO Tell Us?	25
2.2 PEPICO Data Analysis	29
2.2.1 Modeling PEPICO Experiments	29
2.2.2 Quantum Chemical Calculations	34
Chapter 3: Results and Discussion	37
3.1 3,3,3-Trifluoropropene (TFP) and <i>cis</i> -1,2,3,3,3-Pentafluoropropene (PFP)	37
3.1.1 Background and Literature Review	37
3.1.2 Methods	40
3.1.3 Results and Discussion	43
References	68

LIST OF TABLES

Table

1. Summary of Experimental and Calculated (G4) Appearance Energies (E_0) for the Lowest-Energy Fragment Pathways of 3,3,3-Trifluoropropene	47
2. Auxiliary and Derived Thermochemical Data for 3,3,3-Trifluoropropene	53
3. The Most Important Experimental and Calculated (G4) Appearance Energies (E_0) for the Lowest-Energy Fragmentation Pathways of <i>cis</i> -1,2,3,3,3-Pentafluoropropene	59
4. Auxiliary and Derived Thermochemical Data for <i>cis</i> -1,2,3,3,3-Pentafluoropropene	63

LIST OF FIGURES

Figure

1. Sketch of the dissociative threshold photoionization process of a neutral molecule (AB).....	18
2. The original detector designed by Sztáray and Baer in 2003 to resolve the hot electron contamination in PEPICO. ¹⁷	21
3. Diagram depicting the simplified setup of our TPEPICO experiments.....	23
4. Threshold Photoelectron spectrum (TPES) of 3,3,3-trifluoropropene (blue) fit using a Franck–Condon simulation (red) in the 11.0–12.0 eV energy range.	43
5. Breakdown diagram of 3,3,3-trifluoropropene over the 11.8–16.0 eV photon energy range. Experimental data (open shapes) are fit by modeled breakdown curves (solid lines). Experimental 0 K appearance energies (E_0) of the lowest-energy channels are denoted with solid arrows.	44
6. TOF peak center-of-gravity analysis for the m/z 95 H-loss fragment channel in the 12.0–13.0 eV photon energy range.	47
7. Rearrangements of the molecular ion that are involved in the lowest-energy dissociation processes. Values refer to G4 energies in eV and the numbers on the arrows correspond to the transition states connecting these structures.....	49
8. Potential energy surface for the lowest-energy dissociation pathways of 3,3,3-trifluoropropene with the corresponding G4 energies.	50
9. Isomerization of the molecular ion 3,3,3-trifluoropropene with G4 thermochemical limits and transition states.....	50
10. TFP Higher energy H-loss, F-loss, and CF_3 -loss fragment mechanisms. All energies are 0K and calculated at a G4 level of theory.....	51
11. Thermochemical cycle of 3,3,3-trifluoropropene (TFP) system and corresponding H-, F- CF_2 - and CF_3 -loss pathways. The ionization energy of TFP and the 0 K appearance energies of the fragments are experimentally derived and shown in blue. New thermochemical values determined in this work are shown in purple and literature values are shown in red. The 0 K heats of formations used in this cycle are shown in Table 2.....	54

12. Threshold photoelectron spectrum (TPES) of *cis*-1,2,3,3,3-pentafluoropropene (blue) taken in the 10.6–11.6 eV photon energy range, shown together with a Franck–Condon simulation (red dashed trace). 56
13. Breakdown diagram of *cis*-1,2,3,3-pentafluoropropene over the 12.0–16.5 eV photon energy range. Experimental breakdown curves (open shapes) were fit by a statistical model (solid lines). Derived 0 K appearance energies (E_0) are denoted by solid arrows. 57
14. Isomerization of the molecular ion *cis*-1,2,3,3,3-pentafluoropropene with G4 thermochemical limits and transition states. 60
15. Potential energy surface for *cis*-1,2,3,3,3-pentafluoropropene for the lowest energy dissociation pathways with corresponding G4 calculated energies. 60
16. PFP Higher energy H-loss, F-loss, CF_2 -loss, and C_2HF -loss fragment mechanisms. All energies are 0K and calculated at a G4 level of theory. 63
17. Thermochemical cycle of *cis*-1,2,3,3,3-pentafluoropropene (PFP) system and its corresponding CF_2 -loss pathway. The ionization energy of PFP and the 0 K appearance energy of the fragment are experimentally derived and shown in blue while new thermochemical values determined in this work are shown in purple and literature values are shown in red. The 0 K heats of formations used in this cycle are shown in Table 4. 64

LIST OF ABBREVIATIONS

AIE	Adiabatic Ionization Energy
ATcT	Active Thermochemical Tables
B3LYP	Becke–3-parameter–Lee–Yang–Parr exchange-correlation functional
CRF-PEPICO	Combustion Reaction Followed by Photoelectron Photoion Coincidence Spectroscopy
DFT	Density Functional Theory
eV	Electronvolt
FWHM	Full Width at Half Maximum
HFC	Hydrofluorocarbon
HFO	Hydrofluoroolefin
IE	Ionization energy
iPEPICO	imaging Photoelectron Photoion Coincidence Spectroscopy
IRC	Intrinsic Reaction Coordinate
KE	Kinetic Energy
MCP	Microchannel Plate
MS/MS	Multiple-start/Multiple-stop
ms-TPES	mass-selected Threshold PhotoElectron Spectrum
PEPICO	PhotoElectron Photoion Coincidence Spectroscopy
PES	PhotoElectron Spectroscopy or Potential Energy Surface
PFP	<i>cis</i> -1,2,3,3,3-pentafluoropropene
PIMS	PhotoIonization Mass Spectrometry
PST	Phase Space Theory

QCISC	Quadratic Configuration Interaction Size-Consistency method
QET	Quasi-Equilibrium Theory
RRKM	Rice–Ramsperger–Kassel–Marcus theory
SSACM	Simplified Statistical Adiabatic Channel Model
SS/SS	Single-start/Single-stop
STQN	Synchronous Transit-Guided Quasi-Newton
TOF	Time-of-Flight
TFP	3,3,3-trifluoropropene
TPEPICO	Threshold Photoelectron Photoion Coincidence Spectroscopy
TPES	Threshold PhotoElectron Spectrum
TS	Transition State
VMI	Velocity Map Imaging
VUV	Vacuum UltraViolet radiation
ZKE	Zero Kinetic Energy

CHAPTER 1: INTRODUCTION

Photoionization of a neutral molecule can be studied with photoionization mass spectrometry (PIMS) or photoelectron spectroscopy (PES), but both techniques offer a limited amount of information about the photoionization event because they only focus on half of the event and disregard the other half. In the case of PIMS, only the ion is analyzed and for PES, only the electron is analyzed. This downfall can be compensated by utilizing Photoelectron Photoion Coincidence Spectroscopy (PEPICO), which is a combination of both PIMS and PES. PEPICO is able to collect the photoions and photoelectrons in coincidence with each other while providing even more information on the gas-phase system than just PIMS or PES alone. PEPICO can provide highly accurate thermochemical and kinetic data on gas-phase systems while also giving insight to the dissociation mechanisms of these systems. In this work the gas phase dissociative photoionization of two fluorinated propenes, 3,3,3-trifluoropropene (TFP) and *cis*-1,2,3,3,3-pentafluoropropene (PFP), will be discussed utilizing PEPICO spectroscopy.

This study began as an expansion on previous work of another unsaturated hydrofluorocarbon, *trans*-1,3,3,3-tetrafluoropropene (ElixClean).¹ All three of these hydrofluoroolefines are fourth-generation man-made refrigerants and propellants and have lower global warming potential than their predecessors and zero ozone depleting potential.^{2,3} The aim of this study was to expand on the previous work of ElixClean and to gain insight into how the different number of fluorine atoms affects the dissociation mechanisms for each molecule. Modeling the breakdown curve created from plotting the experimental fractional ion abundances over each photon energy with statistical rate theories with the dissociation rates from the time-of-

flight (TOF) mass spectra or a center-of-mass (COM) Gaussian deconvolution reveal thermochemical and kinetic data about the systems.

I will first discuss PEPICO spectroscopy in detail by giving relevant theoretical background and basic principles requires to understand this technique. The next section of my thesis will then explain how to analyze experimental data and model it before I present experimental data on the two hydrofluoroolefines I have studied. For my experimental data, I will give a detailed analysis of the experimental data followed up with a summary of these hydrofluoroolefines.

CHAPTER 2: THEORY AND TECHNIQUES

2.1 Photoelectron Photoion Coincidence Spectroscopy (PEPICO)

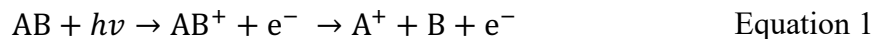
This chapter will describe PEPICO in detail along with the relevant theories and techniques it utilizes. The first subchapter will describe the photoionization process involved in PEPICO experiments and then the detection techniques that are used. The next portion of this subchapter will explain much of the information that can be extracted from PEPICO experiments and how it can be utilized. The second subchapter includes a detailed description of the PEPICO data analysis, including the modeling of experimental data, statistical theories, and quantum chemical calculations.

2.1.1 The Photoionization Process

As previously stated, photoelectron photoion coincidence (PEPICO) spectroscopy is a combination of photoionization mass spectrometry (PIMS) and photoelectron spectroscopy (PES). All three techniques utilize vacuum ultraviolet (VUV) light to ionize a neutral gas phase molecule and then eject an electron if the absorbed photon has enough energy. The first PEPICO instruments utilized a monochromatic VUV light source⁶, such as helium and neon discharge lamps, but most more modern instruments utilize a synchrotron light source that provides tunable VUV light.⁷ Tunable VUV light is required for TPEPICO experiments to ionize and fragment neutral molecules.^{8,9} Tunable synchrotron radiation is produced when electrons moving at almost the speed of light are forced to change trajectory by either a bending magnet, wiggler or undulator.^{10,11} Bending magnets will generate a broad spectrum of wavelengths, so they must be used with a grazing incidence grating monochromator in order to filter out unwanted photon energies. Wigglers and undulators have alternating dipole magnets that force electrons to

oscillate when they travel through them.¹¹ This oscillation produces VUV radiation with an intense light in a narrow energy range.

The different dissociation reactions of the photoion as a function of its internal energy can be studied with these techniques by varying the photon energy and thus, the internal energy of the photoion that is created. The dissociative photoionization process can be shown as:



where AB is the neutral molecule, $h\nu$ is the photon energy absorbed by the molecule, AB^+ is the molecular ion that is formed from this ionization process, and e^- is the electron that is ejected.¹²

The adiabatic ionization energy (AIE) is the minimum energy required to make the neutral molecule into a molecular ion. Once the energy of the absorbed photon is more than the AIE, photoionization can occur. If the molecular ion (AB^+) has enough internal energy, it can undergo fragmentation to produce the fragment ion A^+ and neutral fragment B. This is also represented visually in Figure 1. The energy where fragmentation is possible even starting from an originally zero internal energy neutral molecule, is known as the 0K appearance energy (E_0). This appearance energy is important in modeling the fragmentation of the molecular ion and will be further discussed in detail later. When a molecule AB absorbs a VUV photon with the energy $h\nu$ above the ionization energy (IE), then the ejected electron can have an energy that ranges from 0 to $h\nu - IE$.

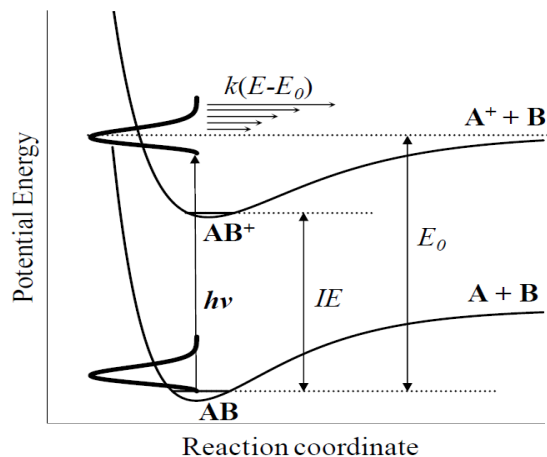


Figure 1. Sketch of the dissociative threshold photoionization process of a neutral molecule (AB).

When there is no reverse barrier in the dissociative photoionization process, such as the dissociation in Figure 1 depicts, then the appearance energy (E_0) and 0K heats of formation ($\Delta_f H_{0K}$) of the precursor molecule (AB), fragment ion (A^+), and neutral fragment (B) are related to each other through this thermochemical equation:

$$E_0 = \Delta_f H_{0K}[A^+] + \Delta_f H_{0K}[B] - \Delta_f H_{0K}[AB] \quad \text{Equation 2}$$

If two of the heat of formations are known, the third can be calculated when the appearance energy (E_0) is measured experimentally. Therefore, the PEPICO technique has been utilized to determine accurate heats of formations for many gas phase species.^{13, 14}

The energetics for the ionization process can be summed up by this equation:

$$E_{ion} = hv - IE - KE + E_{thermal} \quad \text{Equation 3}$$

where E_{ion} is the internal energy of the ion that is produced in the photoionization process, hv is the photon energy, IE is the ionization energy of the neutral precursor molecule, KE is the kinetic energy of the photoelectron that is produced (which is zero in Threshold PEPICO, or TPEPICO), and $E_{thermal}$ is the thermal energy of the neutral molecule before it dissociates.¹³ This equation utilizes the principle of the conservation of energy and assumes $hv < E_0$. The photon energy (hv)

is experimentally controlled by the monochromator. If the ionization energy of the neutral precursor is not known from literature, it can either be experimentally measured or estimated by high level quantum chemical calculations.

The thermal internal energy distribution ($E_{thermal}$) of a neutral sample at T temperature can be calculated by utilizing the Boltzmann formula as shown in Equation 4,

$$P(E) = \frac{\rho(E)e^{\frac{-E}{k_B T}}}{\int_0^\infty \rho(E)e^{\frac{-E}{k_B T}}} \quad \text{Equation 4}$$

where k_B is the Boltzmann constant and $\rho(E)$ is the ro-vibrational density of states function for the neutral. (Note that in the mass spectrometry literature, internal energy is considered excluding the kinetic energy.)

In an ionization event of a PEPICO experiment, the photoions are mass analyzed in a Wiley McLaren time-of-flight (TOF) mass analyzer, where the start signal is provided for by the electron. To study the internal energy of selected photoions, the kinetic energy of the photoelectron must be measured accurately and the photoions and photoelectrons from the same precursor must correctly correspond to each other. Both stipulations can be accomplished through the utilization of threshold photoelectron photoion coincidence (TPEPICO) spectroscopy. The advantage of TPEPICO is that only threshold electrons (those with zero kinetic energy) are detected in coincidence with their corresponding photoions, therefore allowing the internal energy of the ions to be selected accurately.^{1, 8, 9, 15-21}

The experiments presented herein on the dissociative photoionization of 3,3,3-trifluoropropene (TFP) and *cis*-1,2,3,3,3-pentafluoropropene (PFP) were carried out on the prototype CRF-PEPICO (combustion reactions followed by photoelectron photoion coincidence

spectroscopy) endstation of the vacuum-ultraviolet (VUV) beamline at the Swiss Light Source of the Paul Scherrer Institut in Switzerland.⁵

2.1.2 Electron Detection in PEPICO and the “Hot Electron” Problem

Hot electrons are energetic electrons with non-zero kinetic energy. If these hot electrons have velocity vectors that are in the direction of the detector center, then they will be detected along with the threshold electrons (electrons with zero kinetic energy), leading to the “hot electron problem”. In theory, an ion should dissociate at a certain photon energy, but because the hot electrons partition some of the available photon energy, the ion has less internal energy and therefore may not dissociate until higher photon energies.¹⁷

In modern PEPICO spectroscopy, the detection of electrons is based off velocity map imaging (VMI).²² In 1997, Eppink and Parker²³ developed VMI by improving the photofragment ion imaging method that was created by Chandler and Houston.²⁴ VMI is able to distinguish particles based off their initial velocity because those with zero initial kinetic energy will be focused onto the center of the detector while particles with some initial velocity will be focused onto concentric rings whose radii are proportionate to their initial velocities perpendicular to the extraction axis.

The first PEPICO experiment that applied this VMI technique was done by Li and Baer in 2002.¹⁸ Because VMI focuses threshold electrons to a small spot on the detector from a large ionization region, it also allowed them to increase threshold electron signal by a factor of 10 while also increasing the threshold electron kinetic energy resolution by more than a factor of 4. Although this technique does decrease the hot electron contamination of the threshold electron signal, it does not completely solve the problem. This is because some hot electrons may have a kinetic energy vector that is parallel to the extraction axis and therefore will still be detected in

the center of the detector. Previously, there was no way to distinguish between these hot electrons and threshold zero kinetic energy electrons in the center of the detector, but in 2003, Sztáray and Baer developed a solution.¹⁷

Their solution was to include a multichannel plate (MCP) detector with two separate anodes in their instrumental apparatus (Figure 2). One anode would detect only hot electrons on the ring while the other anode would detect the threshold and hot electrons in the center.

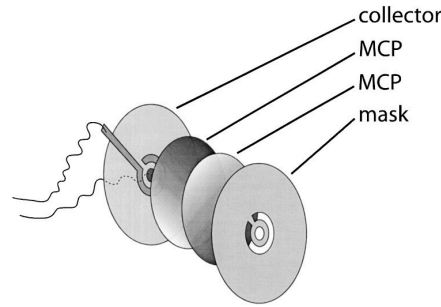


Figure 2. The original detector designed by Sztáray and Baer in 2003 to resolve the hot electron contamination in PEPICO.¹⁷

This allowed them to determine the signal only from the threshold electrons by subtracting the ring signal (only hot electrons) from the center signal (both hot and threshold electrons) and scaling for differences in their areas through an experimentally derived factor (f), as shown in Equation 5 and Equation 6.

$$\text{Threshold signal} = (\text{center signal}) - f \times (\text{ring signal}) \quad \text{Equation 5}$$

$$f \cong \frac{A_1}{A_2} \quad \text{Equation 6}$$

The areas of the center and ring are denoted as A_1 and A_2 , respectively. The factor (f) is only an approximation because it depends on the distribution of electron kinetic energies. Because these energies can vary between experiments, the factor usually needs slight adjustment in order to

account for all of the total hot electron contamination. In imaging PEPICO, the size and position of the center and ring on the detector can be selected to optimize for the best resolution.

2.1.3 Ion Detection in PEPICO

In most PEPICO experiments, ions are mass analyzed by a two-stage Wiley-McLaren type time-of-flight (TOF) mass spectrometer and are space focused onto a multichannel plate detector.^{25,26} This setup allows for a good mass resolution despite the photoions being extracted from a large ionization region with a constant electric field. Without the two-stage Wiley-McLaren setup, since there is a wide spacial distribution of ions of the same mass (isomass ions), their flight times could also have a wide distribution. However, in Wiley-McLaren mass analysis, the isomass ions that are closer to the beginning of the extraction region will have a short acceleration distance and lower kinetic energy when they enter the field free drift region than compared to isomass ions that are extracted further from the ionization volume. Therefore, the latter will eventually catch up with the slower-flying ions that were formed closer to the detector, minimizing the spread in time of flight due to the distribution of ionization positions. After the ions have been separated by their time-of-flight, they are detected by a microchannel plate detector. A reflectron can be added to the PEPICO instrument, in order to increase mass resolution, but careful consideration must be used as some of the ion signal may be lost as a result of this addition.

2.1.4 Coincidence Detection in Threshold PEPICO

The previous subchapters mentioned how photoions and photoelectrons can be detected through TPEPICO spectroscopy, this subchapter will elaborate on how coincidence detection is implemented in the instruments we use at the Swiss Light Source. Samples are introduced into the spectrophotometer via an infusive inlet or molecular beam. The gas phase samples are then

intersected and ionized with the monochromatic VUV synchrotron radiation. This creates photoions and photoelectrons which are then extracted with electric fields (-800V and +120 V) into opposite directions and detected at opposite ends of the PEPICO spectrometer (Figure 3). The electron flight tube (to the left) is 265 mm long and has a 20 mm wide opening to velocity map image the electron beam onto a Roentdek DLD40 position sensitive delay-line detector.^{23,27} Photoelectrons with zero kinetic energy (ZKE) will hit the center of the imaging detector and will be considered in coincidence events. As explained previously, hot electrons with some kinetic energy may be detected both in the center of the detector and also on concentric rings around the center, which is used to account for their contribution to the threshold electron signal. As depicted in Figure 3, photoions are extracted to the right and are mass analyzed as they are separated based on their time-of-flight. They will go through two extraction regions (with the first being 5.5 cm long and the second being 1 cm long) prior to a 55 cm long drift region before being space-focused onto a Jordan TOF C-726 microchannel plate detector.

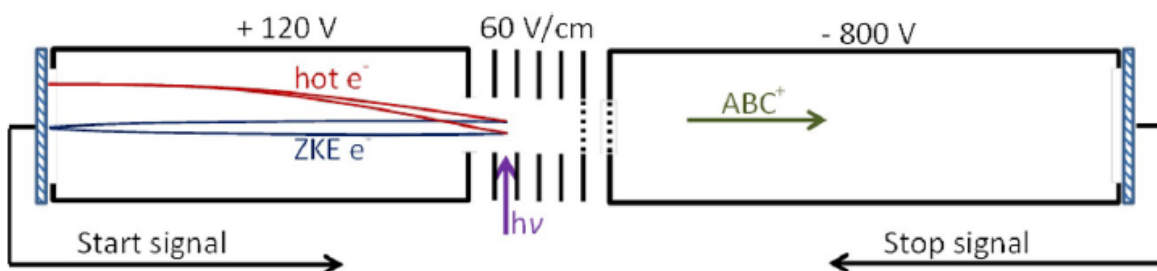


Figure 3. Diagram depicting the simplified setup of our TPEPICO experiments.

Because the photoelectrons have a very small mass, they will hit the detector almost immediately after photoionization. These photoelectrons will give a start signal for the time-of-flight measurement and the ions will give a stop signal and the time difference between the start

and stop signals is the time-of-flight of the corresponding photoion.²⁸ When the electron and ion are from the same precursor molecule, this is called a true coincidence. A false coincidence is when an ion and electron from two different ionization events are paired together, because by chance they happened to be detected within the chosen coincidence detection window, even though they were coming from different ionization events. True coincidences will give time-of-flight peaks that are around the same value whereas the false coincidences will be evenly distributed throughout the whole time-of-flight measurement window. This creates a background with random noise (from the false coincidences) and distinguished time-of-flight peaks (from the true coincidences).

For a single-start/single-stop (SS/SS) coincidence scheme, the electron signal starts the measurement and then the first ion detected will stop the measurement. While the time-of-flight measurement is active, other electrons are not detected until the measurement is restarted. When ionization rates are low, the ionization events are well separated, so this electron-ion pair will be the only one formed in the time-of-flight window of the measurement, and therefore determining the coincidence pair is relatively straightforward. The first PEPICO spectrophotometers had low ionization rates due to the limitation of light intensity of laboratory-based VUV light sources.²⁹ When ionization rates are higher, ionization events begin to overlap, thus causing the incorrect electron-ion pairing from different ionization events. Consequently, the SS/SS coincidence scheme cannot be utilized efficiently because there may be too many false coincidences being detected relative to the true coincidences, thus creating a spectrum that is undecipherable.

When the ionization rate is over 10 kHz, one needs to use the multiple-start/multiple-stop (MS/MS) data acquisition scheme.^{30,31} In this scheme, all threshold electrons and ions will be detected with all their times relative to a master clock.^{28,31} Each electron will then be correlated

with each ion and the false coincidences will create a flat background while the true coincidences will have a true time-of-flight peak. This data acquisition scheme can be utilized even with ionization rates as high as 10^6 s^{-1} .

The signal-to-noise ratio (S/N) due to the false coincidence background for a coincidence peak is independent of the ionization rate (because the Poisson-noise of the false coincidence count rates is proportional to the square root of the square of the ionization rate, while true coincidences are also directly proportional to the ionization rate). Therefore, to boost the signal-to-noise ratio, it is best to have long collection times, narrow peak widths, and high collection efficiencies but not arbitrarily high count rates.

In PEPICO, ionization events create electrons and ions in pairs and because these are detected in coincidence it is possible to determine collection efficiencies. The electron and ion collection efficiencies (η_e and η_i) can be determined from the total coincidence count rate (N_c) and the measured electron and ion count rates (N_e and N_i , respectively) through these equations:

$$\eta_e = \frac{N_c}{N_i} \quad \text{Equation 7}$$

$$\eta_i = \frac{N_c}{N_e} \quad \text{Equation 8}$$

Being able to determine η_e and η_i can aid in optimizing the spectrometer to have the best collection efficiency possible for the experiment. The total ionization rate (N_T) of the experiment can be determined once the electron and ion collection efficiencies are known (Equation 9).

$$N_T = \frac{N_e}{\eta_e} = \frac{N_i}{\eta_i} \quad \text{Equation 9}$$

2.1.5 What Can TPEPICO Tell Us?

PEPICO spectroscopy can give a wide range of information on gas phase systems including thermodynamic, kinetic, and spectroscopic data along with mechanistic dissociative

photoionization reactions. All PEPICO experiments provide information to create a breakdown diagram, which is a plot of the fractional ion abundances as a function of photon energy.

Fractional ion abundances are found by integrating the corresponding TOF peaks in the TOF mass spectrum. At higher photon energies, the energy distribution is also shifted to higher energies, so there is a higher probability for more dissociation to occur.

A breakdown diagram gives information about the appearance energy (E_0) of fragment ions, which can then be used in thermochemistry to obtain the heats of formations of the neutral molecule and fragment ions. Since TPEPICO only considers zero energy electrons, the ion internal energy (E_{ion}) can be calculated by:

$$E_{ion} = h\nu - AIE + E_{thermal} \quad \text{Equation 10}$$

where $h\nu$ is the photon energy, AIE is the adiabatic ionization energy of the neutral, and $E_{thermal}$ is the thermal energy distribution. When the precursor neutral molecule has more thermal energy it requires less photon energy to dissociate. The energy at which the molecular ion completely fragments and has an ion signal of zero is also known as the 0 K appearance energy of the fragment ion. This is when the photon energy equals the appearance energy of the fragment ion (E_0) and the whole energy distribution is above the dissociation limit. In the breakdown diagram, the slopes of the fractional ion abundances reflect the internal energy distribution. This is a function of temperature, so with lower temperatures the initial thermal energy distribution is narrower. This is reflected in the breakdown diagrams with a steeper slope.

Breakdown diagrams can also help visualize and quantitate the mechanisms for the dissociative photoionization of the molecule.³² They can help determine if a dissociation is parallel or consecutive or if there is more than one channel contributing to a specific ion signal.⁸ Parallel dissociations are when fragment ions come from the same molecular ion while

consecutive dissociations are when a fragment ion can undergo further fragmentation. When more than one channel contributes to a fragment ion, then there will be a notable change in slope of the breakdown diagram (*vide infra*, in Chapter 3).

When there is only one fast dissociation channel, the relative fragment ion abundance will be based off what portion of molecular ion energy distribution has enough excess energy to dissociate. In a fast dissociation, at the E_0 (the appearance energy of the fragment ion), the fragment ion will have a relative abundance of 100% whereas the molecular ion's relative abundance will be 0%. When the dissociation is slow or there are more than one parallel dissociation channels present, then the dissociation rates must also be taken into account as a function of internal energy. The rates can be extrapolated to E_0 values for their corresponding fragment ions and aid in accurately modeling all relative fragment ion abundances in the experimental data.

PEPICO experiments also provide kinetic information in the ion time-of-flight peak shapes and position.^{8, 14, 33} When a dissociation is slow, it creates a metastable fragment ion peak that is asymmetrical. The unimolecular rate constants can be extracted from the mass spectra by fitting this asymmetrical time-of-flight peak. The range for measuring ion dissociation rates is typically between 10^4 - 10^7 s⁻¹. This range can be increased by changing the extraction field settings or by adding onto the instrumental apparatus. The addition would include a deceleration region after the first flight tube in the Wiley-McLaren type mass analyzer and a second, shorter drift region.

A molecular ion will dissociate at a different position in the Wiley-McLaren time-of-flight mass spectrometer depending on the unimolecular rate of the molecular ion's dissociation. A fast dissociation occurs when all molecular ions dissociate once there is enough excess internal

energy to do so. In fast dissociations, the appearance energy corresponds to when the molecular ion signal reaches zero. Fast dissociations result in sharp peaks in the TOF spectra due to the fragment ions having the same flight time. On the other hand, slow dissociations create metastable asymmetric fragment ion TOF peaks. This is because the metastable molecular ion will dissociate while it is traveling through the first extraction region. The ion's total time of flight will be based off where the dissociation occurs within this region. If it occurs towards the beginning of the extraction region, the time-of-flight will be shorter. The time-of-flight values will range between the fragment ion's flight time and the intact molecular ion's flight time, thus creating a quasi-exponential TOF peak that changes shape based off the rate constant of the dissociation. The dissociation rate ($k(E)$) can be modeled when the thermal distribution of the sample is considered, and these rate curves can be fitted to the asymmetrical peak shapes with the geometry of the spectrometer and the applied voltages. The appearance energy can be accurately determined by extrapolating the energy where the dissociation rate reaches the minimum value.

The higher the size of the molecule, the more likely a slow dissociation is to occur because there is a finite rate at which energy flow occurs between all the vibrational-rotational modes in a polyatomic ion. This results in a kinetic shift, which will cause the experimental appearance energy of a fragment to be shifted to higher photon energies because at threshold the time for the molecular ion to fully dissociate is larger than the timeframe of the experimental TOF window.³⁴⁻³⁹ Kinetic shifts are accounted for quantitatively as the TOF peak shapes give absolute dissociation rates. It is important to understand dissociation kinetics because this allows you to determine accurate appearance energy values and to calculate correct heats of formations.

As TPEPICO focuses on threshold electrons, a threshold photoelectron spectrum can be created by plotting the detected threshold electron signal as a function of photon energy. In this spectrum, peaks will represent the system going into another ionic state with the first peak representing the experimental adiabatic ionization energy (AIE) of the neutral molecule being studied. TPEPICO can also provide a mass-selected threshold photoelectron spectra (ms-TPES) by only looking at threshold photoelectrons that are in coincidence with a specific ion mass-to-charge ratio. This feature allows one to also obtain the threshold photoionization spectra of various neutrals in a mixture. These can be utilized as spectral fingerprints to identify the neutral by comparing to spectra in literature or simulated TPES from Franck-Condon calculations.

As noted, PEPICO spectroscopy is a combination of PES and PIMS, but it is truly greater than the sum of its parts and exceeds both techniques in the abundance of information that can be obtained.

2.2 PEPICO Data Analysis

This subchapter will focus on how PEPICO experimental data is analyzed. I will first provide a detailed description of how the experimental data is modeled with statistical thermodynamics. The following section will then focus on quantum chemical calculations and its application in PEPICO experiments

2.2.1 Modeling PEPICO Experiments

In 2010, *Sztáray et al.* published the details of the PEPICO data analysis software and made it available to the scientific community.¹⁴ This code can model the experimental data (the breakdown diagram and the ion TOF distributions) utilizing statistical thermodynamics. Modeling the experimental data can aid in determining accurate kinetic and thermochemical data for the studied system.

The program calculates the density of states functions to model the experimental data when provided with the vibrational frequencies and rotational constants (from quantum chemical calculations) for the neutral, all the ions, and transition states if there are any. Once this is determined, the program can then calculate the thermal energy distribution of the neutral precursor. During ionization it is assumed that this thermal energy distribution is transferred to the ionic manifold, so thus the molecular ion's internal energy ($E(M^+)$) can be calculated by:

$$E(M^+) = E(M) + h\nu - IE \quad \text{Equation 11}$$

where $E(M)$ is the internal energy of the molecular neutral, $h\nu$ is the photon energy, and IE is the ionization energy of the molecular neutral. Dissociation will occur when the internal energy of the molecule is larger than the dissociation energy.

Kinetic models aim to describe the energy dependence of the rate constant for a system using the smallest number of parameters possible.⁴⁰ The modeling code provided by *Sztáray et al.* can use different unimolecular rate theories, but only one will be focused on here as it is the only one utilized in this thesis.

The Rice-Ramsperger-Kassel-Marcus (RRKM) theory can be utilized to successfully model the kinetics for unimolecular reactions from just a few parameters.⁴¹⁻⁴⁶ This theory was initially developed by Rice, Ramsperger⁴⁴⁻⁴⁶ and Kassel⁴⁶ who based their work off Hinshelwood's research⁴⁷ but was later corrected by Marcus and Rice in 1951⁴³ and Rosenstock, Warrhaftig, and Eyring in 1952.⁴⁸ This theory is also sometimes referred to as the Quasi-Equilibrium Theory (QET). The advantage of using the RRKM theory to model experimental data is that even with minimum prior knowledge of the system it can still provide accurate and reliable results.

Unimolecular reactions are often first-order reactions. When modeling with RRKM theory, the unimolecular rate constant ($k(E)$) can be calculated as:

$$k(E) = \frac{\sigma N^\ddagger(E - E_0)}{h\rho(E)} \quad \text{Equation 12}$$

where σ is the reaction degeneracy, $N^\ddagger(E - E_0)$ is the number of states of the transition state at $(E - E_0)$ excess energy above the dissociation limit, h is Plank's constant, and $\rho(E)$ is the precursor ion density of states. When modeling with RRKM theory, $N^\ddagger(E - E_0)$ is calculated from the fixed vibrational frequencies from the transition state structure involved in the reaction. How to determine the transition state structures will be further discussed in the next subchapter.

Some systems may have parallel and consecutive dissociations.⁸ In a consecutive dissociation, a fragment ion (AB^+) from one dissociation will further fragment into another ion and neutral for another consecutive dissociation scheme (Equation 13).



It's important to know the internal energy distribution after the first dissociation, in order to model the consecutive reaction, since the ion AB^+ becomes a precursor ion for the consecutive dissociation. The internal energy distribution of AB^+ can be calculated from the internal energy distribution of the original molecular ion (ABC^+) while taking into consideration how the excess energy after dissociation ($E - E_0$) is split between the fragments (AB^+ and C), as seen in Equation 14.

$$E - E_0 = E_i + E_n + E_{translational} \quad \text{Equation 14}$$

The internal energy of the ion and neutral fragments, AB^+ and C , are represented by E_i and E_n , respectively, and $E_{translational}$ represents the translational energy released. The ion AB^+ will have a wider internal energy distribution than compared to the molecular ion ABC^+ .

Since the partition of excess energy after dissociation has been considered, the internal energy distribution of AB^+ can now be calculated for each energy in the product ion's energy distribution $P(E)$ and summed over the molecular distribution. This can be calculated as:

$$P(E_i, E - E_0) = \frac{\rho_{AB^+}(E_i) \int_0^{E-E_0-E_i} \rho_C(x) \rho_{tr}(E - E_0 - E_i - x) dx}{\int_0^{E-E_0} \rho_{AB^+}(y) (\int_0^{E-E_0-y} \rho_C(x) \rho_{tr}(E - E_0 - y - x) dx) dy} \quad \text{Equation 15}$$

where $P(E_i, E-E_0)$ is the probability of the fragment ion to have E_i energy from the total excess energy from $E-E_0$ and ρ_{AB^+} , ρ_C , and ρ_{tr} are the density of states of the fragment ion AB^+ , neutral fragment C , and translational degrees of freedom, respectively.^{49, 50} Once the fragment ion's internal energy distribution is determined, it can be used to find the energy dependent rate constants for consecutive dissociations.

The next step of the modeling program involves modeling the breakdown diagram and TOF distributions. As stated previously, the breakdown diagram is created by integrating the TOF peaks and plotting the fractional ion abundances as a function of photon energy. This is modeled by using all the previously calculated ion energy distributions and dissociation rates for each dissociation in the experiment. The breakdown curve of the molecular ion is photon energy dependent and is calculated as:

$$BD(h\nu) = \int_0^{E_0-I E} P(E, h\nu) dE + \int_{E_0-I E}^{+\infty} P(E, h\nu) \exp(-k(E)\tau_{max}) dE \quad \text{Equation 16}$$

Equation 16 ensures the breakdown curve accounts for the effect of slow dissociations with the second integral. For fast dissociations, the relative abundance will only depend on the normalized internal energy distribution (E) at a given photon energy ($h\nu$) and the second term in Equation 16 is zero. In other words, the molecular ion abundance is given by the area of the internal energy distribution that is below the dissociation limit (E_0). As stated previously in Equation 4 the width of the distribution is dependent on the temperature of the sample for fast

dissociations, but the appearance energy of the fragment ion (E_0) is not temperature dependent. For slow dissociations, the internal energy dependent rate constant $k(E)$ can be found by utilizing Equation 12. Equation 16 also can account for kinetic shift in the experimental data by incorporating the probability that the molecular ion does not dissociate within a time window, τ_{max} . The time is based on the experimental geometry and extraction field.

The fragment ion breakdown curves ($BD_{frag}(h\nu)$) can therefore be calculated by taking into consideration that the molecular ion and fragment ion abundance must equal 1, as seen in Equation 17.

$$BD_{frag}(h\nu) = \int_{E_0-E}^{+\infty} P(E, h\nu) (1 - \exp(-k(E)\tau_{max})) dE \quad \text{Equation 17}$$

If there is more than one parallel dissociation, then for a specific fragment ion (i), the breakdown curve (BD) can be calculated as:

$$BD_i(h\nu) = \int_{E_0-IE}^{+\infty} P(E, h\nu) \frac{k_i(E)}{\sum_j k_j(E)} \left(1 - \exp - \left(\sum_j k_j(E)\tau_{max} \right) \right) dE \quad \text{Equation 18}$$

where $\frac{k_i(E)}{\sum_j k_j(E)}$ is the branching ratio between the fragment ion (i) and all the other fragment ions (j) in the experiment.

For slow dissociations, the TOF distributions must also be modeled along with the breakdown diagram for the dissociation rates. Modeling the peak shapes will reveal the energy dependent unimolecular rate constant ($k(E)$) in asymmetric fragment ion peaks.

In the modeling program different parameters (such as appearance energy, temperature, vibrational frequencies for the transition states, and peak widths) are optimized to find the best fit of the experimental data (the breakdown diagram and the TOF spectra).

2.2.2 Quantum Chemical Calculations

Quantum chemical calculations are very important in PEPICO data analysis. As noted above, they provide vibrational frequencies and rotational constants for the stationary points on a potential energy surface for the model and aid in studying all the possible dissociation mechanisms of the photoionization process.

Our typical analysis of experimental data is aided by *ab initio* calculations that are carried out using the Gaussian 09 suite of programs.⁵¹ All PEPICO quantum chemical calculations presented in this work begin with optimizing the neutral molecule and molecular ion with a Density Functional Theory (DFT)^{52, 53} method based on B3LYP (Becke, 3-parameter, Lee-Yang-Parr) hybrid functional.⁵⁴⁻⁵⁸ The vibrational and rotational frequencies from these optimizations can then be extracted and used as input parameters for the modeling code to calculate the internal energy distribution.

Since the fragment ions were mass analyzed, their m/z values are known. Integrating their TOF peaks and plotting against photon energy creates a breakdown diagram that experimentally reveals the order of which these fragment ions appear. Based off the m/z values and order of appearance, a rough dissociation scheme showing all the possible mechanisms can be drafted and all the possible fragments (ions and their corresponding neutrals) for each m/z value are then optimized with a B3LYP level of theory. The energetics of each fragment can be extracted from these optimizations. Calculating the energy difference between the precursor and the fragments gives the thermochemical limit for each reaction dissociation. This thermochemical limit is the minimum energy required to form the fragment ion and neutral. Some of the possible mechanisms can be eliminated at this point if their thermochemical limits are significantly higher than the experimental appearance energies in the breakdown diagram.

For the remaining reactions, transition state (TS) structures from the precursor to the fragment ion are located by using relaxed potential energy scans along the bond breaking reaction coordinates. The local maximum (if any) is then optimized as a transition state and the vibrational frequencies are used as an input for the model. If a transition state cannot be found this way, then the Synchronous Transit-Guided Quasi-Newton (STQN) method is used instead.^{59,60} This method searches for a saddle point along the potential energy surface between the optimized reactant and product ion structures. With both methods, if a transition state is identified, then an intrinsic reaction coordinate (IRC)⁶¹ calculation is run to prove that the TS is the local maximum from the reactant to the product. If a TS still cannot be found, then this indicates that the dissociation reaction happens on a purely attractive potential energy surface that does not involve a reverse barrier. Since RRKM theory requires TS vibrational frequencies as inputs in the model, such a loose transition state can be approximated by stretching the bond corresponding to the dissociation reaction coordinate to 4-5 Å long.

All the B3LYP energetics in the potential energy surface can then be further refined with G4 composite method.⁶² This can accurately determine bond dissociation energies for systems that have a relatively low number of heavy atoms by extrapolating to the infinite basis full configuration interaction limit by using different levels of theory and basis sets. Composite methods are utilized to decrease computational cost while still maintaining a relatively high accuracy. They use approximations to estimate the electron correlation energy and the energies from translation, rotations, and vibrations while also correcting for non-considered correlation effects.

Quantum chemical calculations aid in analyzing experimental data by playing a critical role in divulging the different dissociation mechanisms for the photoionization process. The

thermochemical limits from these quantum chemical calculations can be compared to experimentally derived appearance energies to find the ones that agree, revealing the most likely dissociation mechanisms for that system.

CHAPTER 3: RESULTS AND DISCUSSION

3.1 3,3,3-Trifluoropropene (TFP) and *cis*-1,2,3,3,3-Pentafluoropropene (PFP)**3.1.1 Background and Literature Review**

The Montreal Protocol (1987) restricted the use of chemicals with a high ozone depleting potential (ODP), which were replaced by hydrofluorocarbon refrigerants with sometimes high global warming potentials (GWP). The Paris Accord (2016) aims at limiting the use of these high GWP substitutes and has led to the development of new alternatives⁶³ with lower GWP and zero ODP.⁶³⁻⁶⁵ Hydrofluoroolefins (HFOs), such as 3,3,3-trifluoropropene (TFP) and *cis*-1,2,3,3,3-pentafluoropropene (PFP), have shorter atmospheric lifetimes and, thus, a lower GWP, and recently been introduced to the market. These fourth-generation refrigerants have numerous commercial applications and are more environmentally friendly than chlorofluorocarbons (CFCs) or hydrochlorofluorocarbons (HCFCs). Their shortened lifetime is due the carbon–carbon double bond in HFOs, which increases their reactivity.

The gas-phase reaction of *cis*-1,2,3,3,3-pentafluoropropene and other HFOs have been studied with some main tropospheric oxidants (Cl, OH, and NO₃) to understand their degradation mechanism in the atmosphere.^{64,65} It has been concluded that increasing in the number of fluorine atoms increases the rate coefficient for the reaction with OH.⁶⁵ Therefore, the GWP of HFOs is considered negligible due to their short atmospheric lifetimes.^{64,65} The negligible GWPs and low ODPs that make these compounds environmentally favorable.

Previous studies on the ionic dissociation processes of 3,3,3-trifluoropropene (TFP) included ab initio calculations, electron ionization, and photoionization mass spectrometry studies. The ionization energy of TFP has been estimated as 10.95 eV with the help of

calculated isodesmic reaction energies,⁶⁶ 11.24 ± 0.04 eV based on electron ionization mass spectrometry (EI-MS) results,⁶⁷ and 10.9 eV using photoionization mass spectrometry (PI-MS).⁶⁸ The EI mass spectrum shows prevalent peaks for H-, F-, C₂H₃-, C₂H₂F-, CF₂-, CF₃- and CHF₃- loss dissociations. Bond dissociation and appearance energies of these fragments have also been reported.⁶⁷ This study highlighted that TFP exhibits ionic dissociations that can only happen through rearrangements, and that this species, similar to tetrafluoropropene,⁶⁹ shows an intense fluorine-loss peak in the mass spectra.⁶⁷ The TFP heat of formation has been reported at 298 K as -648.52 kJ/mol,⁶⁷ -614.2 ± 6.7 kJ/mol,⁷⁰ and -621.8 ± 1.6 kJ/mol,⁷¹ but these values are inconsistent with one another. The ionic dissociation of PFP has not been previously studied with photoionization or other high energy-resolution mass spectrometry.

This study is an extension of our recent PEPICO (photoelectron photoion coincidence) spectroscopy work on another fluorinated propene, *trans*-1,3,3,3-tetrafluoropropene,⁶⁹ another fourth-generation man-made refrigerant and propellant, commercially referred to as HFO-1234ze. Through a threshold photoelectron spectrum (TPES), an adiabatic ionization energy was reported, and we have observed three parallel dissociation channels from internal energy selected parent ions: H-loss, F-loss, and CF₂-loss pathways. This study noted that even though direct bond breaking dissociations were possible, several of the lowest energy pathways involved hydrogen or fluorine shifts prior to dissociation, in order to form the more energetically favored allylic structure for the fragment ions. While the lowest-energy fluorine loss did occur directly, hydrogen- and fluorine-shift isomerization was required for the observed H-loss and CF₂-loss dissociation channels. At slightly higher energies, several rearrangement pathways became accessible, due to the high mobility of the fluorine atom, and these all contributed to the observed dissociation channels. According to density functional and G4 calculations, most of

the low-energy fragment structures were allylic fragment ions, showing extensive H and F scrambling.

Hexafluoropropene (C_3F_6), a closely related perfluorinated analogue to the hydrofluoroolefins TFP and PFP studied here, was studied with photoionization mass spectrometry^{72,73} and photoelectron photoion coincidence (PEPICO) spectroscopy.⁷⁴ The adiabatic ionization energy was reported as 10.6 ± 0.2 eV. This study noted that the CF_3 group on the propene reduces the π nature of the carbon-carbon double bond, therefore increasing the perfluoro effect and the stability of the highest occupied molecular orbital in the neutral. Hexafluoropropene has four low-energy parallel dissociative ionization channels: F loss, CF_2 loss, C_2F_3 loss, and C_2F_5 loss. At higher energies, a consecutive dissociation channel was observed: the loss of F + C_2F_4 . Some of these reactions have to be preceded by fluorine atom migration.

In this paper, the dissociative photoionization of 3,3,3-trifluoropropene and *cis*-1,2,3,3,3-pentafluoropropene was studied with threshold PEPICO spectroscopy below a photon energy of 16.5 eV. This study aims to expand on previous work of hydrofluoroolefins, exploring the rearrangement and dissociation processes of the energy selected ions, while also updating literature thermochemical values. From previous studies, it can be hypothesized that we will observe H-loss, F-loss, CF_2 -loss, and CF_3 -loss dissociations, and possibly a C_2F_3 -loss channel in PFP. We also expect to see evidence for the migration (scrambling) of the hydrogen and fluorine atoms, leading to fragments that cannot be formed through direct dissociation of the molecular ion.

3.1.2 Methods

3,3,3-trifluoropropene and *cis*-1,2,3,3,3-pentafluoropropene were purchased from abcr GmbH and used without further purification. The experiments were conducted at the prototype CRF-PEPICO endstation of the VUV beamline at the Swiss Light Source of the Paul Scherrer Institut.⁵ Only a summary of the CRF-PEPICO apparatus is given here as further detailed information is available elsewhere.⁷⁵ The gaseous samples were introduced at room temperature into the ionization region of the experimental chamber of the CRF-PEPICO through a Teflon tube, to reach a chamber pressure of 1.3×10^{-6} mbar. VUV synchrotron radiation was collimated, dispersed by a 600 grooves/mm laminar grating, and focused at the exit slit in a differentially pumped gas filter. The gas filter contained a mixture of Ne and Ar at a pressure of 10 mbar over an optical length of 10 cm to suppress higher order harmonics of the synchrotron light. Ar autoionization lines were used to calibrate the VUV photon energy. The sample was ionized by the monochromatic VUV radiation in the ionization region of the spectrometer in a 2 mm \times 2 mm cross section.

Once ionized, the photoelectrons and photoions were extracted in opposite directions with a constant 220 V cm⁻¹ electric field. Photoions were mass analyzed in a gridless two-stage Wiley–McLaren-type time-of-flight (TOF) mass spectrometer and detected by a fast Roentdek DLD40 delay-line imaging detector. The TOF mass analysis setup consists of a 2.7 cm long extraction, 8.7 cm long acceleration, and an 88.6 cm long field free drift region. Photoelectrons were velocity map imaged onto a Roentdek DLD 40 position-sensitive delay-line detector with better than a 1 meV electron kinetic energy resolution at threshold. Threshold electrons have zero kinetic energy and were detected in the center of the image while energetic (“hot”) electrons only contribute to the center signal if they have zero off-axis momentum. Since they are also

detected elsewhere on the velocity map image, their contribution to the center signal can be accounting for by the average count rate in a concentric ring area around the center and scaling it by an experimentally determined factor.¹⁷ The photoelectrons provide the start signal for the time-of-flight (TOF) measurement in a multi-start/multi-stop coincidence scheme, while the photoions provide the stop signals.³¹ After the TOF mass analysis, a breakdown diagram is constructed by plotting the fractional abundances of ions in coincidence with threshold photoelectrons as a function of photon energy.²⁹

The low extraction field in the long extraction region allows ion residence times on the order of microseconds. With these conditions, any metastable molecular ion with unimolecular dissociation rates between 10^3 - 10^7 s⁻¹ will give asymmetrical fragment ion peaks in the time-of-flight mass spectra while a fast dissociation of the molecular ions will produce symmetric fragment ion peaks.^{8, 14, 33} In the case of a hydrogen loss from a heavy molecular ion, such as from either of the studied fluoropropenes, the small mass difference does not allow for complete separation of the TOF peaks. In this work, this issue was resolved by fitting the TOF peaks with Gaussian functions to obtain the fractional ion abundances, while the center-of-gravity (CoG) of the combined peaks was used to assess the effect of slow dissociation by quantifying the asymmetry of the hydrogen-loss peak, as described above.^{19, 76, 77}

Computational

Ab initio calculations were carried out with the Gaussian 09 suite of programs to assess the various isomerization/dissociation pathways, as well as to provide input parameters for the statistical rate analysis of the experimental data.⁵¹ The minimum-energy structures for the neutral precursors, the molecular ions, the possible fragment ions, as well as the identified isomerization products were optimized at the B3LYP/6-311++G(d,p) level of theory. For the

dissociative pathways, transition state (TS) structures were located by constrained optimization by scanning along the reaction coordinate (loose TS) and by Synchronous Transi-Guided Quasi-Newton (STQN) calculations (tight TS).^{78,79} Verification of these latter transition states was done by intrinsic reaction coordinate (IRC) calculations, confirming the minimum-energy structures that the saddle points connect.⁶¹ The energies of all identified minima and saddle points were then further refined with the G4 composite method.⁸⁰ Rotational constants and harmonic vibrational frequencies were calculated for all of these critical points (and approximate loose TS structures), to be used as input for the statistical mechanical modeling. The experimental adiabatic ionization energy can be determined from the experimental TPES by fitting Franck-Condon-simulated theoretical spectrum to it. These calculations were done at the B3LYP/6-311++G(d,p) level of theory for TFP and M06-2X/def2-TZVPP level of theory for PFP.

Statistical Modeling

The unimolecular rate constants of each dissociative pathway were calculated with the (rigid activated complex, rac-) Rice–Ramsperger–Kassel–Marcus (RRKM) theory as implemented in our PEPICO modeling code, as described earlier.^{14,81} The rate constant, $k(E)$, as a function of energy (E) is calculated with the following formula:

$$k(E) = \frac{\sigma N^\ddagger(E - E_0)}{h\rho(E)} \quad \text{Equation 19}$$

where σ is the symmetry number of the reaction, $N^\ddagger(E - E_0)$ is the number of states function for the transition state at internal energy ($E - E_0$), h is Plank's constant, $\rho(E)$ is the density of states of the dissociating ion at an internal energy E . The densities and numbers of states were calculated using harmonic vibrational frequencies by the Beyer–Swinehart direct count algorithm.⁸²

3.1.3 Results and Discussion

For clarity, the numbering convention from here onwards is the following: the 3,3,3-trifluoropropene molecular ion is labeled **1a**, while its isomers and fragment ions are listed as **2a**, **3a**, etc. The *cis*-1,2,3,3,3-pentafluoropropene (**1b**) isomers and fragment ions are labeled as **2b**, **3b**, etc.

3,3,3-trifluoropropene

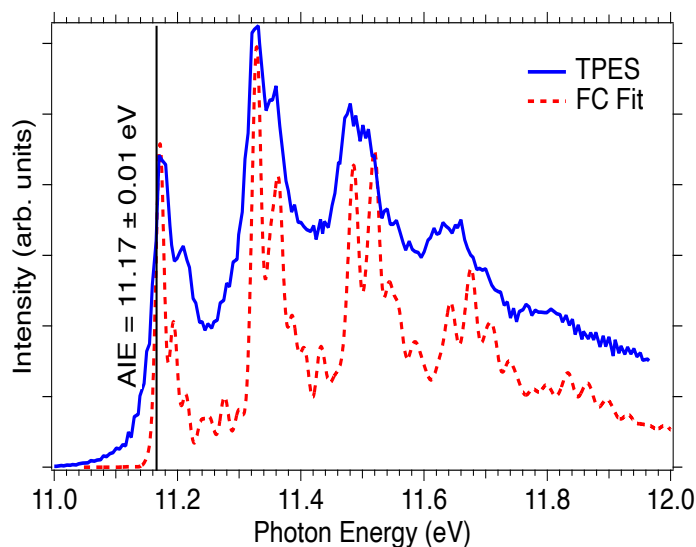


Figure 4. Threshold photoelectron spectrum (TPES) of 3,3,3-trifluoropropene (blue) fit using a Franck–Condon simulation (red) in the 11.0–12.0 eV energy range.

The ground-state band of the threshold photoelectron spectrum (TPES) of 3,3,3-trifluoropropene is shown in the 11.0–12.0 eV photon energy range in Figure 4, together with results of a Franck–Condon simulation at the M06-2X/def2-TZVPP level, convoluted with 60 cm^{-1} fwhm Gaussians to account for the rotational envelope and the spectral resolution. By varying the adiabatic ionization energy, the ionization energy of the FC simulation was shifted to

reproduce the experimental TPES best. The experimental adiabatic ionization energy is, thus, determined as 11.17 ± 0.01 eV.

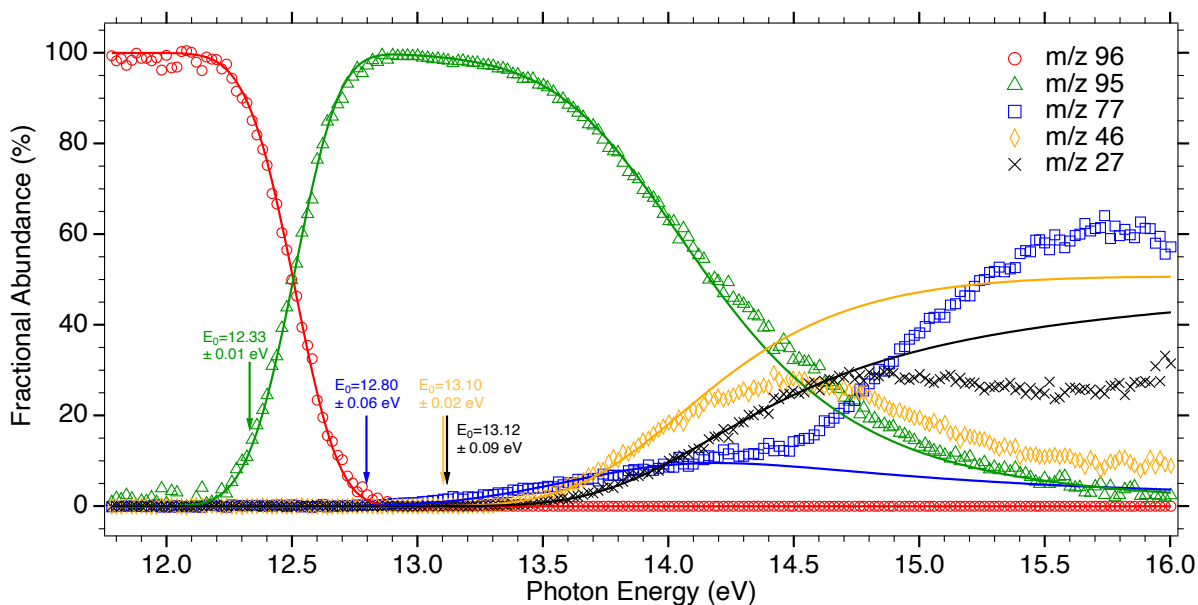


Figure 5. Breakdown diagram of 3,3,3-trifluoropropene over the 11.8–16.0 eV photon energy range. Experimental data (open shapes) are fit by modeled breakdown curves (solid lines). Experimental 0 K appearance energies (E_0) of the lowest-energy channels are denoted with solid arrows.

Threshold photoionization time-of-flight mass spectra of 3,3,3-trifluoropropene was measured over the photon energy range of 11.8–16.0 eV. The integrated peak areas in the coincidence time-of-flight mass spectra were converted to ion fractional abundances and plotted as a function of photon energy to create the breakdown diagram as shown in Figure 5. Within the energy range of the experiment, there are four main fragment ions at m/z 95, 77, 46, and 27. The m/z 95 fragment ion corresponds to hydrogen loss from the molecular ion and appears at 12.2 eV. This fragment ion reaches 100% abundance and then begins to decrease slowly as other

dissociation channels open at higher photon energies. As shown later, the formation of the m/z 95 H-loss fragment ion requires rearrangement prior to dissociation at its onset energy.

The m/z 77 fragment ion corresponds to 19 amu, *i.e.*, fluorine atom loss. Based on the change of slope in the breakdown curve at 14.5 eV, at least two active dissociation pathways contribute to this channel. We will show that fluorine atom loss can occur (1) in the direct dissociation of a fluorine–carbon bond in the original 3,3,3-trifluoropropene molecular ion at a lower energy or (2) from an isomer parent ion at higher photon energy. This is consistent with our previous work on tetrafluoropropene, which confirmed that rearrangement processes were involved in the fluorine-loss dissociative ionization in that system.⁶⁹

The m/z 46 ion corresponds to CF₂ loss. Clearly, this dissociation cannot occur through direct bond scission of the 3,3,3-trifluoropropene molecular ion and requires rearrangement prior to dissociation, similarly to the analogous channel in tetrafluoropropene.⁶⁹

The m/z 27 fragment ion corresponds to the loss of a trifluoromethyl radical. Over the studied energy range, this reaction likely proceeds through more than one mechanism, as there is a marked increase in the slope of the breakdown diagram around 15.8 eV. Theoretically, this dissociation channel can occur through a direct bond scission from the molecular ion, but this fragment ion is also available through a consecutive dissociation channel, losing a CF₂ moiety from the F-loss fragment ion (m/z 77). The existence of this latter, consecutive channel is supported by the experimental breakdown diagram because as the m/z 27 ion fractional abundance begins to increase around 15.5 eV, the abundance of the m/z 77 fragment ion starts to decrease with around same rate.

The statistical dissociative ionization model to reproduce the experimental data used the measured adiabatic ionization energy of 11.17 eV and a sample temperature of 300 K (Figure 5).

In the absence of a reverse barrier, the 0 K appearance energy (E_0) corresponds to the thermochemical limit to dissociative ionization. Otherwise, it gives us the energy of the rate-limiting transition state of the fragmentation. The best fit of the model to the experimental breakdown curve (Figure 5) and the center-of-gravity curve (Figure 6) (for the H-loss dissociation, carrying information about the dissociation kinetics) was obtained by optimizing E_0 and the transitional TS frequencies for each dissociation channel. The model fits the experimental data very well up to a photon energy of 14.0 eV. As shown later with the help of quantum chemical calculations, there are numerous possible dissociation channels at higher energies that may or may not contribute to fragmentation. This multitude of energetically open pathways lead to a convoluted fragmentation mechanism, in which the individual channels and their contributions cannot be unambiguously identified. Similarly complex high-energy fragmentation mechanism was also observed in fluoropropene, an analogous HFO,⁶⁹ and can best be unveiled using potential energy surface exploration by computational chemistry. The lowest-energy structures involved in the dissociation processes, are summarized in Table 1 along with their energetics. Further possible structures with higher energies are shown with their mechanism in Figure 10.

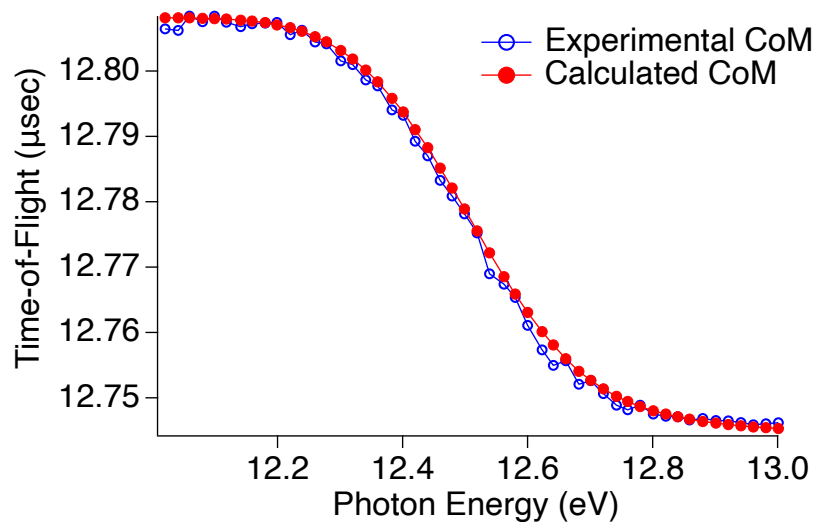


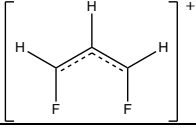
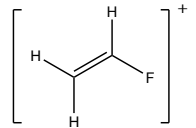
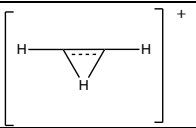
Figure 6. TOF peak center-of-gravity analysis for the m/z 95 H-loss fragment channel in the 12.0–13.0 eV photon energy range.

Table 1

Summary of Experimental and Calculated (G4) Appearance Energies (E_0) for the Lowest-Energy Fragment Pathways of 3,3,3-Trifluoropropene

m/z	Fragment Ion Structure	Neutral Fragment	E_0 (eV)	
			Experimental	G4
95		H	12.33 ± 0.01	12.24
				12.29
77		F	12.80 ± 0.06	12.77
				12.97
				13.04

(Table 1 Continued)

				13.10
46		CF ₂	13.10 ± 0.02	13.32
27		CF ₃	13.12 ± 0.09	13.14

The first fragment ion, C₃H₂F₃⁺ (*m/z* 95), appears at 12.2 eV. As mentioned earlier, the experimental mass resolution was not sufficient for baseline separation the molecular ion [M]⁺ (*m/z* 96) and the H-loss fragment ion [M – H]⁺ (*m/z* 95) peaks, as is commonly the case for H-loss processes. A Gaussian-fitting deconvolution was utilized to obtain the ion fractional abundances, while the combined (*m/z* 95 and 95) peaks' center of mass was used to utilized as the experimental information on the dissociation rate constants. The model was simultaneously fitted to the experimental breakdown diagram and the center of gravity curve by optimizing the barrier height, *i.e.*, the dissociation limit, and the two lowest vibrational frequencies of the transition state, corresponding to the transitional modes (Figure 6). The fit provided an H-loss appearance energy of 12.33 ± 0.01 eV, in agreement with the calculated G4 thermochemical limits for the two lowest-energy *m/z* 95 fragment ions of 12.24 and 12.29 eV. Both channels involve a fluorine-atom shift from C3 in the original molecular ion (**1a**) to C1 to form the isomer parent ion **2a**, which subsequently loses a hydrogen from the C1 position (Figure 7 and Figure 8). The cis [**5a**] and trans [**4a**] H-loss fragments are calculated to be close in energy, and probably both are formed in dissociative ionization. A slightly higher-energy H-loss fragment

ion can also be formed by first shifting a fluorine from the C3 position to C2 through an isomerization barrier at 11.97 eV, forming intermediate **[3a]** at 11.53 eV (at the G4 level) (Figure 7). From this structure, the central hydrogen atom can be lost, leading to another allylic structure at 12.80 eV (Figure 10). Other possible higher-energy hydrogen loss products and the mechanisms leading to them are detailed in Figure 9 and Figure 10. It is important to note that the lowest-energy H-loss fragment ions are those that feature an allylic structure, and these can only be formed after a rearrangement of **1a**.

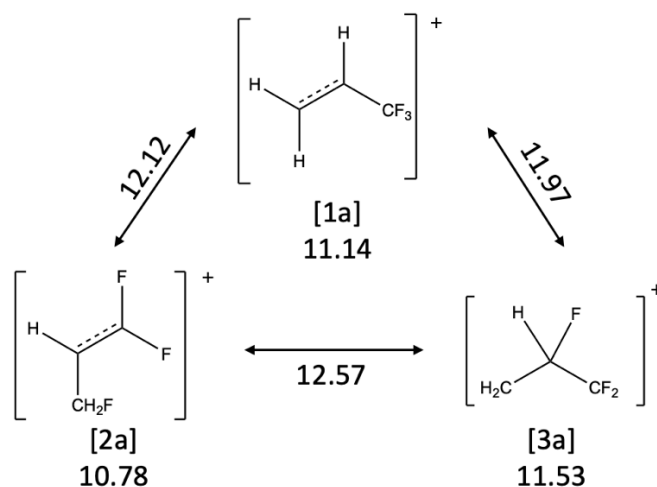


Figure 7. Rearrangements of the molecular ion that are involved in the lowest-energy dissociation processes. Values refer to G4 energies in eV and the numbers on the arrows correspond to the transition states connecting these structures.

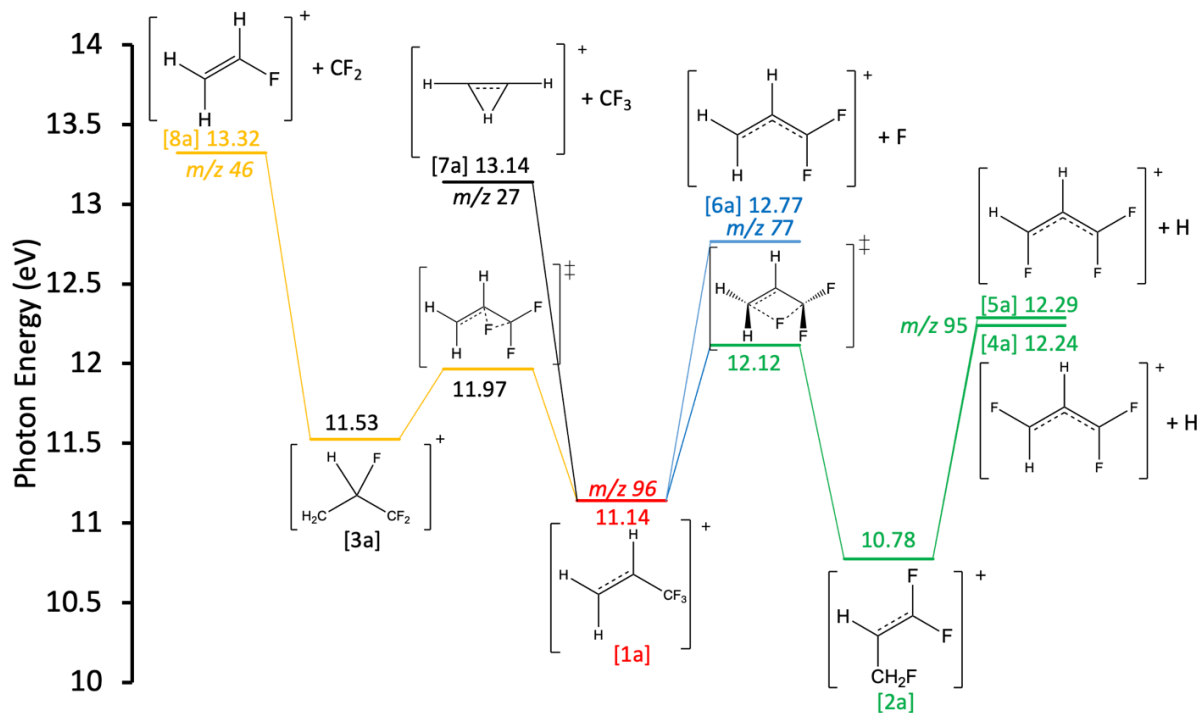


Figure 8. Potential energy surface for the lowest-energy dissociation pathways of 3,3,3-trifluoropropene with the corresponding G4 energies in eV.

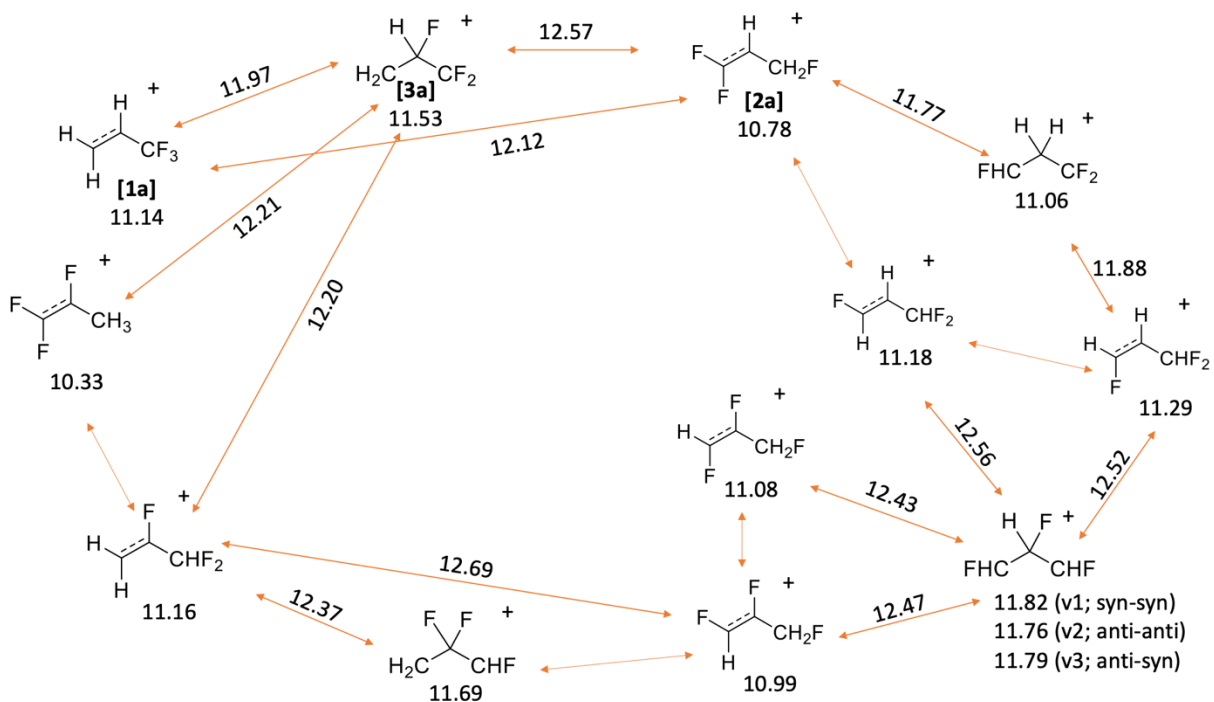


Figure 9. Isomerization of the molecular ion 3,3,3-trifluoropropene with G4 thermochemical limits and transition states.

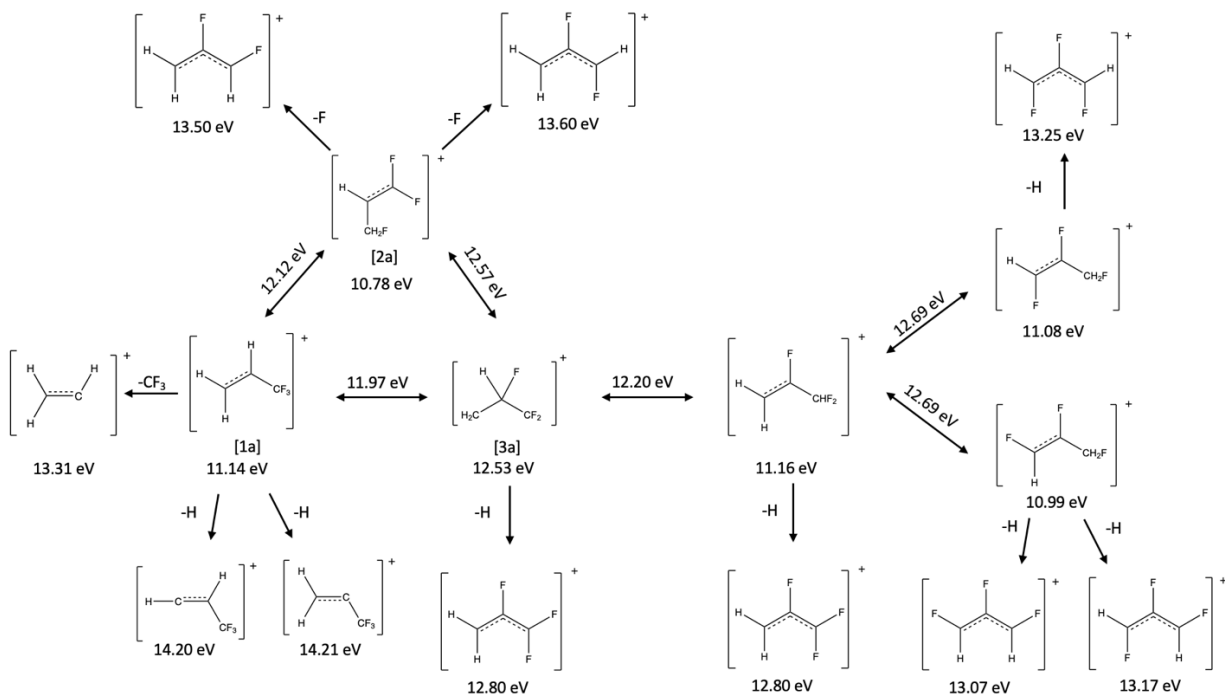


Figure 10. TFP Higher energy H-loss, F-loss, and CF₃-loss fragment mechanisms. All energies are 0K and calculated at a G4 level of theory.

The next dissociation channel, m/z 77, corresponds to $C_3H_3F_2^+$, formed by fluorine atom loss from the molecular ion. The statistical model of the first F-loss channel yielded a 0 K appearance energy of 12.80 ± 0.06 eV. The fragment ion has a stable allylic structure, formed by losing a fluorine atom from the trifluoromethyl group in **1a**. At the G4 level, the calculated thermochemical limit for this channel was found to be 12.77 eV, in excellent agreement with the experimental appearance energy (Figure 8). According to our calculations, there are three more stable allylic $C_3H_3F_2^+$ isomers with similar but slightly higher thermochemical limits (12.97, 13.04, and 13.10 eV at G4 (Table 1)), which may also contribute to the breakdown diagram. Other, higher energy F-loss fragment ions are shown together with their formation mechanism in (Figure 10).

The next two dissociation channels, m/z 46 and m/z 27, correspond to CF_2 and CF_3 loss from the molecular ion, respectively. They are parallel dissociation channels from the molecular ion, with fitted experimental appearance energies of 13.10 ± 0.02 eV and 13.12 ± 0.09 eV at 0 K, respectively. The lowest energy calculated thermochemical limit to form the $\text{C}_2\text{H}_3\text{F}^+$ ion at m/z 46 was calculated to be 13.32 eV, while the thermochemical limit to C_2H_3^+ (m/z 27) formation was found at 13.14 eV. In order to form the lowest energy m/z 46 fragment ion, the fluorine from C3 in the molecular ion **[1a]** must move to the C2 position, similar to the hydrogen-loss mechanism detailed above. From the intermediate **[3a]** at 11.526 eV, the CF_2 group can dissociate to form the fluoroethylene cation at 13.32 eV (G4 value, Figure 8). The latter value is slightly higher than the experimental appearance energy of 13.10 ± 0.02 eV. The m/z 46 fragment ion can also be formed through consecutive F-loss and CF -loss dissociation steps, but the thermochemical limit for this dissociation pathway is calculated to be much higher at 18.63 eV.

The m/z 27 fragment ion, the vinyl cation, C_2H_3^+ , is readily formed by homolytic bond breakage between the C2 and C3 carbons. The calculated thermochemical limit at 13.14 eV (Figure 8) is in excellent agreement with the experimental appearance energy of 13.12 ± 0.09 eV. The vinyl cation has a non-classical structure, in which a bridging hydrogen atom straddles the carbon-carbon double bond.^{9,83,84} At higher energies, a consecutive dissociation pathway may also contribute to the m/z 27 fragment ion signal, namely CF_2 loss from the m/z 77 ($\text{C}_3\text{H}_3\text{F}_2^+$) fragment ion, but the calculated thermochemical limit for this dissociation is much higher (16.78 eV).

As shown in Figure 5, the statistical model reproduces the experiment well under a photon energy of 14.0 eV. Similar to tetrafluoropropene,⁶⁹ several isomerization/dissociation

channels become energetically available due to the vagabond nature of the fluorine atom above this energy. Unfortunately, these channels are not individually identifiable based on the experimental data. Nevertheless, we have mapped several high-energy isomerization/dissociation pathways and these quantum chemical results are summarized Figure 9 and Figure 10.

Thermochemistry

Table 2

Auxiliary and Derived Thermochemical Data for 3,3,3-Trifluoropropene

Formula	Name	$\Delta_f H^\circ_{0K}$	$\Delta_f H^\circ_{298K}$ (kJ mol ⁻¹)	Uncertainty
C ₃ H ₃ F ₃	3,3,3-trifluoropropene	-611.6 ^a	-622.3 ^{a,i}	± 8.4
			-648.52 ^b	
			-604.6 ^c	± 6.7
			-614.2 ^d	± 7
			-621.8 ^e	± 1.6
			-629.8 ^f	± 2.8
C ₃ H ₂ F ₃ ⁺	allylic cation [4a]	362.2 ^a		± 8.5
			364.6 ^g	± 1.4
C ₃ H ₃ F ₂ ⁺	allylic cation [6a]	546 ^a		± 10
C ₂ H ₃ F ⁺	vinyl fluoride ion [8a]	846.6 ^a		± 8.5
C ₂ H ₃ ⁺	bridged vinyl cation [7a]	1119.07 ^h	1115.63 ^h	± 0.55
CF ₃ ·	trifluoromethyl radical	-464.95 ^h	-467.75 ^h	± 0.45
CF ₂	difluoromethylene	-193.89 ^h	-193.42 ^h	± 0.36
H	hydrogen atom	216.034 ^h	217.998 ^h	± 0.000

^aThis work. ^bSteele and Stone⁶⁷ ^cKolesov et. al.⁸⁵ ^dCox and Pilcher.⁷⁰ ^ePaulechka et. al. experimental.⁷¹ ^fPaulechka et. al. calculated.⁷¹ ^gRay and et. al.⁶⁹ ^hActive thermochemical Tables (ATcT).⁸⁶ ⁱConverted to $T = 298$ K using G4 thermal enthalpies.

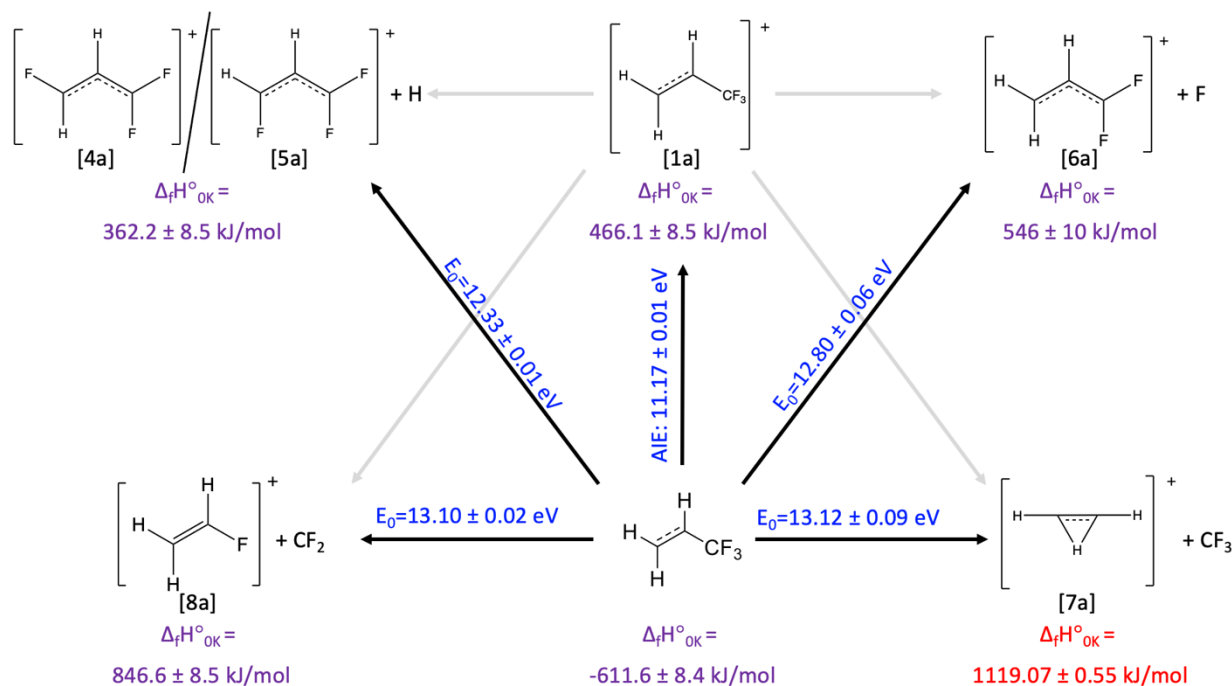


Figure 11. Thermochemical cycle of 3,3,3-trifluoropropene (TFP) system and corresponding H-, F- CF₂- and CF₃-loss pathways. The ionization energy of TFP and the 0 K appearance energies of the fragments are experimentally derived and shown in blue. New thermochemical values determined in this work are shown in purple and literature values are shown in red. The 0 K heats of formations used in this cycle are shown in Table 2.

In the absence of reverse barriers in the dissociative ionization of 3,3,3-trifluoropropene (TFP), the appearance energies correspond to the thermochemical limits even in the presence of isomerization steps in the H-loss and CF₂-loss dissociation pathways (Figure 8). Therefore, the 0 K heat of formation of TFP can be calculated using literature values for the cation and neutral fragments together with the experimental appearance energy. Auxiliary and derived thermochemical data are summarized in Table 2 and Figure 11.

The m/z 27 dissociation channel corresponds to the formation of the vinyl cation (C₂H₃⁺) and a trifluoromethyl radical (CF₃·) loss from the molecular ion [1a]. This dissociation takes place directly in the molecular ion [1a] without isomerization. The heat of formation for both fragments are known, and the heat of formation for the neutral 3,3,3-trifluoropropene,

$\Delta_f H_{0K}(\text{TFP})$, can be derived based on the appearance energy (E_0) of the fragment ion. With the experimental derived $E_0(\text{C}_2\text{H}_3^+) = 13.12 \pm 0.09$ eV and literature values of $\Delta_f H_{0K}(\text{C}_2\text{H}_3^+) = 1119.07 \pm 0.55$ kJ/mol⁸⁶ and $\Delta_f H_{0K}(\text{CF}_3\cdot) = -464.95 \pm 0.45$ kJ/mol⁸⁶, we determine $\Delta_f H_{0K}(\text{TFP}) = -611.6 \pm 8.4$ kJ/mol. Using B3LYP-calculated thermal enthalpies, this heat of formation converts to -622.3 ± 8.4 kJ/mol at 298 K. Previously, the room temperature TFP heat of formation has been reported as -648.52 ,⁶⁷ -614.2 ± 7 ,⁷⁰ and -604.6 ± 6.7 kJ/mol.⁸⁵ The last value was later reevaluated by Cox and Pilcher as -614.2 ± 6.7 kJ/mol in 1970⁷⁰ and again in 2019 by Paulechka and Kazakov⁷¹ as -621.8 ± 1.6 kJ/mol. In the latter paper, they also published a calculated value of -629.9 ± 2.8 kJ/mol. Our value confirms the latest, revised enthalpies of formation reported in the literature.

Based on the newly obtained $\Delta_f H_{0K}(\text{TFP}) = -611.6 \pm 8.4$ kJ/mol, the heats of formation of three parallel primary dissociative ionization products can also be derived using their E_0 and the literature heats of formation of the corresponding neutral fragments, as listed in Table 2. For the H-loss dissociation channel (m/z 95), we can use this method despite the rearrangements because the isomerization barriers are below the thermochemical limit of the dissociation. Thus, we determine the 0 K heat of formation of CHFCHCF_2^+ as 362.2 ± 8.5 kJ/mol. A different dissociative ionization pathway previously yielded 364.6 ± 1.4 kJ/mol⁶⁹ for this value. For the F-loss dissociation channel (m/z 77), the heat of formation for $\text{CH}_2\text{CHCF}_2^+$ was determined as 546 ± 10 kJ/mol. Finally, the dissociation channel yielding the m/z 46 fragment ion corresponds to CF_2 loss. Similar to the H-loss dissociation pathway, there are no reverse barriers as the isomerization barriers are below the thermochemical limit to dissociative ionization. Therefore, we could determine the heat of formation of CH_2CHF^+ as 846.6 ± 8.5 kJ/mol at 0 K. To the best

of our knowledge, the heats of formation of $\text{CH}_2\text{CHCF}_2^+$ and CH_2CHF^+ have not been previously reported.

***cis*-1,2,3,3,3-Pentafluoropropene**

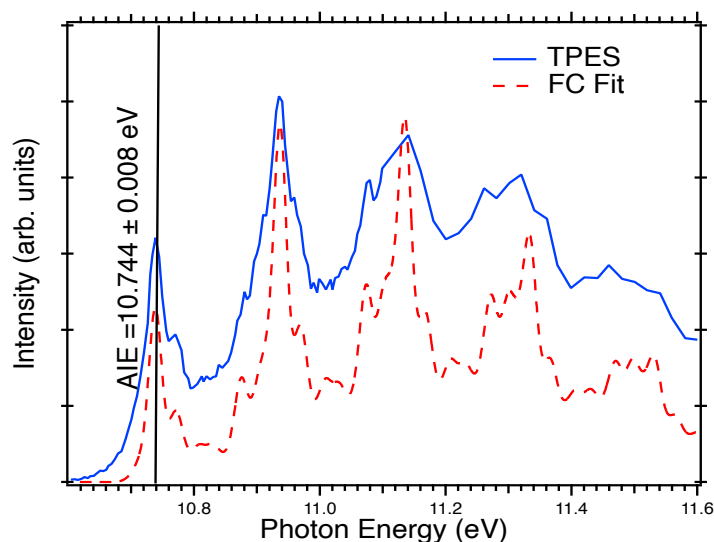


Figure 12. Threshold photoelectron spectrum (TPES) of *cis*-1,2,3,3,3-pentafluoropropene (blue) taken in the 10.6–11.6 eV photon energy range, shown together with a Franck–Condon simulation (red dashed trace).

The adiabatic ionization energy of *cis*-1,2,3,3,3-pentafluoropropene could be determined based on the threshold photoelectron spectrum (Figure 12) and Franck–Condon simulations, carried out on the electronic ground state of the neutral and the cation at the B3LYP/6-311++G(d,p) level of theory. The calculated transitions were convoluted with a Gaussian function with 80 meV FWHM. By varying the adiabatic ionization energy, the calculated spectrum was fit to the experimental TPES. From this, the adiabatic ionization energy was determined to be 10.744 ± 0.008 eV, which was used in the statistical rate model.

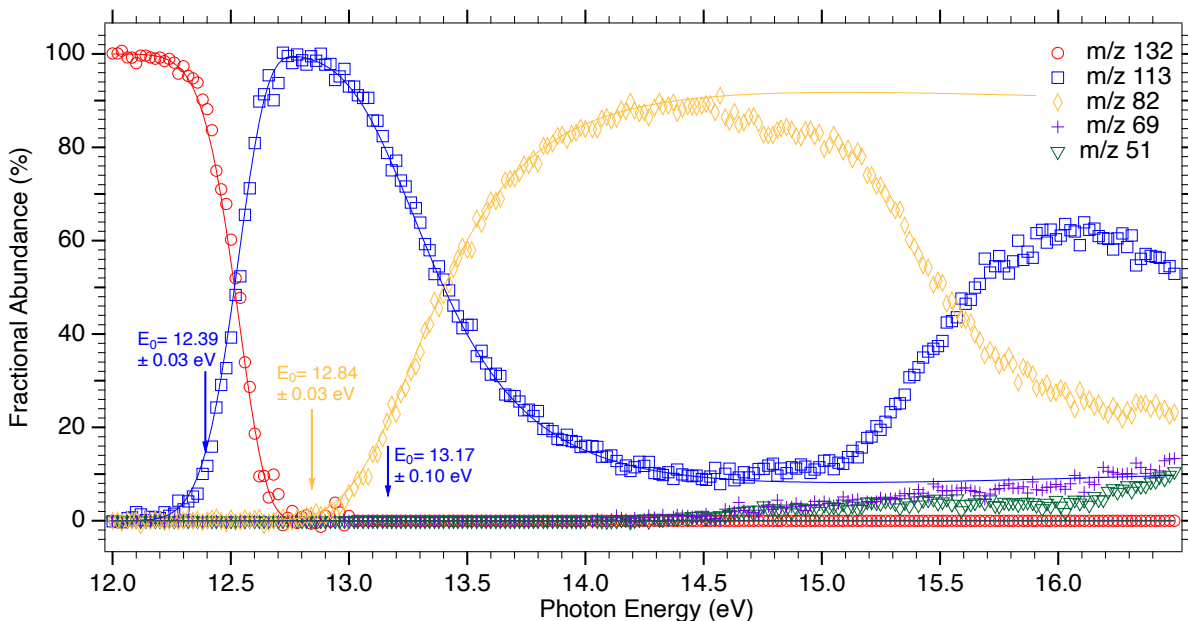


Figure 13. Breakdown diagram of *cis*-1,2,3,3,3-pentafluoropropene over the 12.0–16.5 eV photon energy range. Experimental breakdown curves (open shapes) were fit by a statistical model (solid lines). Derived 0 K appearance energies (E_0) are denoted by solid arrows.

PEPICO time-of-flight spectra of *cis*-1,2,3,3,3-pentafluoropropene was measured over the photon energy range of 12.0–16.5 eV, and the fractional ion abundances (the breakdown curve) are shown in Figure 13. There are four main fragment ions at m/z 113, 82, 69, and 51 within this energy range. At the lowest energies, the only the parent ion is seen at m/z 132. Two further fragment ions were seen at m/z 69 and m/z 51 with a low fractional abundance in the photon energy range of the experiment. These were not included in the statistical model.

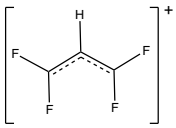
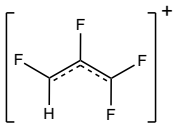
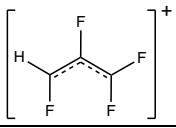
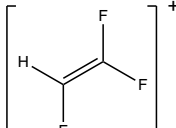
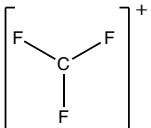
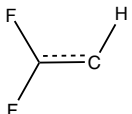
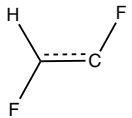
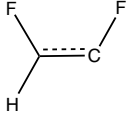

The m/z 113 fragment ion is the first to appear at 12.3 eV and corresponds to a fluorine atom loss from the parent ion. The fractional abundance of this fragment ion begins to decrease as the m/z 82 ion, which corresponds to CF_2 loss from the molecular ion, begins to take over. As was the case with trifluoropropene ion (*vide supra*), this process cannot happen through direct bond scission from the molecular ion but requires isomerization steps along the dissociation coordinate. While the m/z 82 channel quickly outcompetes the fluorine-loss dissociation, it

never reaches 100% abundance. Above 14.5 eV, the fluorine-loss fragment ion begins to increase in abundance again. This experimental finding suggests that there are probably several other fluorine-loss pathways, which open up at higher energies. Above 14 eV, two other parallel fragmentation channels appear, leading to the CF_3^+ (m/z 69) and CHF_2^+ (m/z 51) fragment ions.

The statistical model includes the two lowest-energy channels, corresponding to F and CF_2 loss, at 300 K sample temperature. Like tri- and tetrafluoropropene,⁶⁹ the fluorine atoms become mobile at high energies, leading to multiple competitive pathways to the same products. At these energies, the CF_3^+ and CHF_2^+ channels also become accessible. Although they compete with the main two dissociative pathways, their fractional abundance stays too low for a reliable estimate on their experimental appearance energies. While the statistical model only yields two well-determined appearance energies, we have nevertheless computationally explored several more isomerization pathways. The lowest-energy structures involved and their energetics are summarized Table 3. Possible higher-energy structures and the mechanisms leading to these are shown in Figure 14 and Figure 16.

Table 3

The Most Important Experimental and Calculated (G4) Appearance Energies (E_0) for the Lowest-Energy Fragmentation Pathways of cis-1,2,3,3,3-Pentafluoropropene

Fragment Ion		Neutral Fragment	E_0 / eV	
m/z	Structure		Experimental	G4
113		F	12.39 ± 0.030 13.17 ± 0.10	12.46
				13.19
				13.26
82		CF ₂	12.84 ± 0.03	12.95
69			< 14 eV	13.44
				13.78
				13.80
51	CHF ₂ ⁺		< 14 eV	13.87

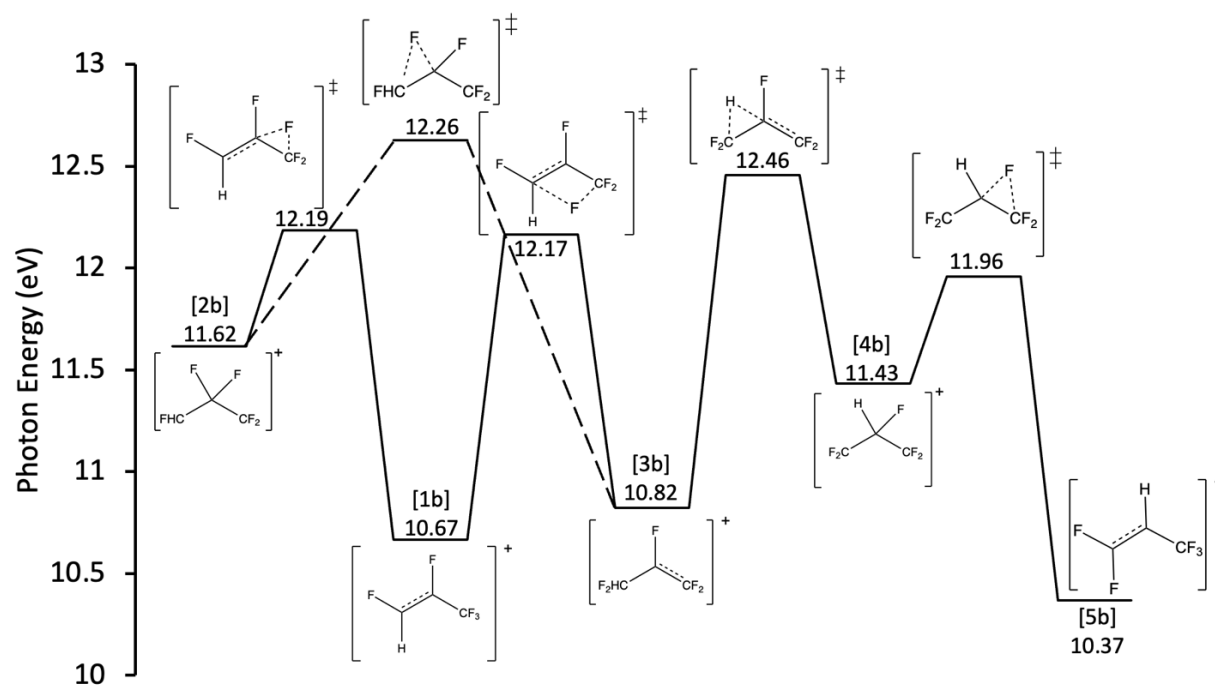


Figure 14. Isomerization of the molecular ion *cis*-1,2,3,3,3-pentafluoropropene with G4 thermochemical limits and transition states.

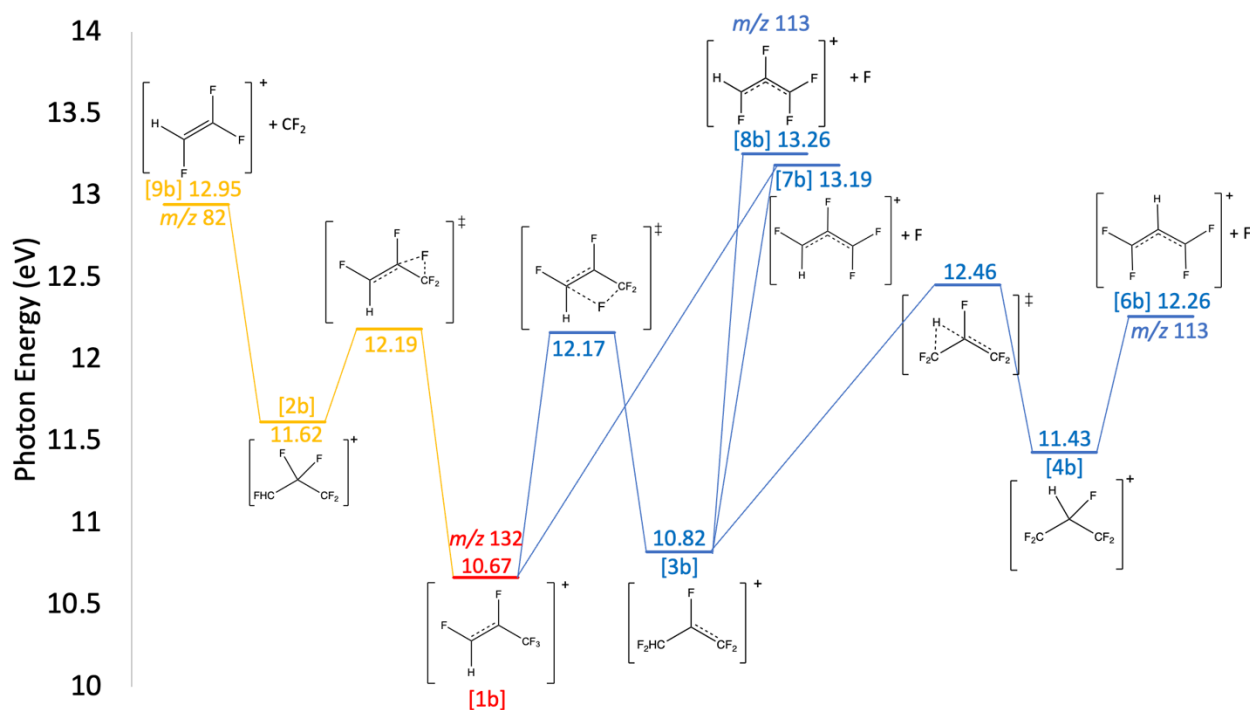


Figure 15. Potential energy surface for *cis*-1,2,3,3,3-pentafluoropropene for the lowest energy dissociation pathways with corresponding G4 calculated energies.

Similar to 3,3,3-trifluoropropene, several *cis*-1,2,3,3,3-pentafluoropropene fragmentation channels also require the molecular ion to isomerize prior to dissociation. The various possible molecular ion isomers and the relevant transition states connecting them are shown in Figure 14. The lowest energy pathway to form the fluorine-loss fragment ion, C_3HF_5^+ , involves a fluorine shift from the C3 to C1 position to form isomerized molecular ion [**3b**], then a hydrogen shift from the C1 to C2, forming [**4b**], prior to losing a fluorine to form the most stable allylic structure $\text{CF}_2\text{CHCF}_2^+$ (Figure 15). The fluorine- and hydrogen-shift transition states are at 12.17 eV and 12.46 eV, respectively, and the latter represents the calculated appearance energy as it is higher than the thermochemical limit at 12.26 eV, all at the G4 level. The experimental appearance energy of 12.39 ± 0.03 eV is in very good agreement with the calculated value of 12.46 eV, further confirming that the lowest-energy, symmetrical allylic structure is indeed formed at low ion internal energies.

At slightly higher energies, calculations suggest that other m/z 113 formation pathways become accessible. Indeed, the experimental breakdown curve and the statistical model both confirm this hypothesis as there is a notable change in slope at ~ 14.5 eV; see Figure 13. Furthermore, without a second fluorine-loss pathway in the model, the fractional abundance of the m/z 113 channel drops to zero too early and the contribution of the m/z 82 channel (vide infra) is overestimated. The appearance energy of this parallel m/z 113 channel was found to be 13.17 ± 0.10 eV. This E_0 value energy is consistent with the calculated thermochemical limit for two other m/z 113 fragment ions structures: [**7b**] at 13.19 eV and [**8b**] at 13.26 eV, which are also allylic structures and *cis/trans* isomers of each other. The former fragment ion can be formed through a direct fluorine loss from the molecular ion, while the latter one is accessible

from the [**3b**] isomer ion. Since the latter one [**8b**] is formed through a submerged transition state, its appearance energy corresponds to the thermochemical limit, just like [**7b**].

The next dissociation channel, yielding the m/z 82 fragment ion, corresponds to CF_2 loss to form the trifluoroethylene cation, C_2HF_3^+ . Since CF_2 loss is not directly available from the molecular ion, the lowest energy pathway involves a fluorine shift from C3 to C2 to form the isomer structure [**2b**], which can then lose the CF_2 moiety. The isomerization barrier is calculated to be at 12.186 eV, significantly lower than the calculated thermochemical limit of 12.947 eV. The experimental appearance energy of 12.84 ± 0.03 eV is in good agreement with the latter.

Above 14.5 eV, the statistical model begins to deviate from the experimental data, as new fluorine-loss dissociation pathways become available. This is in line with our findings for trifluoropropene (vide supra) and tetrafluoropropene,⁶⁹ as the mobile fluorine atoms result in extensive scrambling, followed by dissociation. We have not attempted to model the dissociation channels leading to the m/z 69 and 51 fragment ions, as their abundance never amounts to more than a few percent. Furthermore, calculations show that the CF_3^+ fragment ion can be accompanied by three different neutral fragments in the 13.44–13.80 eV appearance energy range, namely a $\text{CF}_2\text{--CH}\cdot$ and two $\text{CHF--CF}\cdot$ radical isomers, see Table 3.

Another interesting aspect of this system that unlike trifluoropropene and tetrafluoropropene,⁶⁹ the experimental data for pentafluoropropene does not show an H-loss dissociation channel. For the lowest-energy hydrogen loss channel, a fluorine from C3 on the molecular ion [**1a**] must first shift to C1 before the hydrogen can be lost (Figure 16). The G4 thermochemical limit is 12.66 eV, which is within the experimental energy range. However, F

loss takes place at a lower energy of 12.46 eV, explaining why the latter one does not appear in the experimental data.

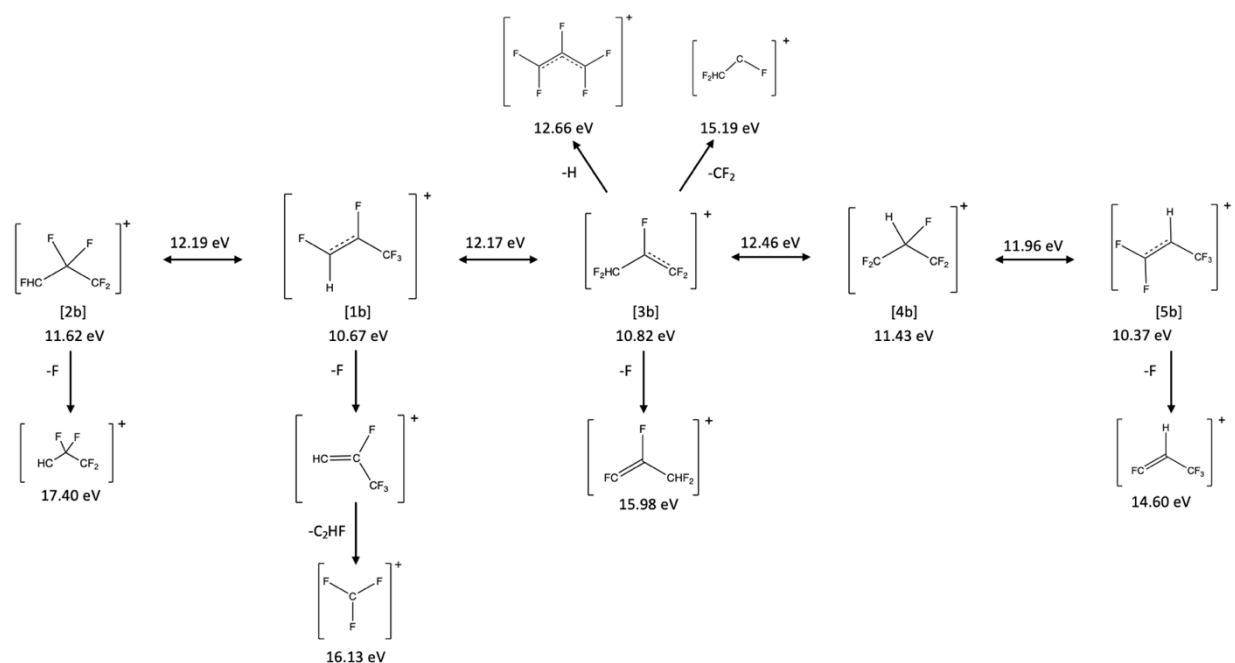


Figure 16. PFP Higher energy H-loss, F-loss, CF_2 -loss, and C_2HF -loss fragment mechanisms. All energies are 0K and calculated at a G4 level of theory.

Thermochemistry

Table 4
Auxiliary and Derived Thermochemical Data for *cis*-1,2,3,3,3 Pentafluoropropene.

Formula	Name	$\Delta_f H^\circ_{0\text{K}}$	$\Delta_f H^\circ_{298\text{K}}$ (kJ mol ⁻¹)	Uncertainty
C_3HF_5	<i>cis</i> -1,2,3,3,3-trifluoropropene	-948.3 ^a	-955.8 ^a	± 5.3
C_2HF_3	trifluoroethylene	-493.8 ^b	-499.1 ^b	± 4.4
C_2HF_3^+	trifluoroethylene cation [9b]	484.4 ^a		± 4.4

(Table 4 Continued)

CF₂ difluoromethylene -193.89^c -193.42^c ± 0.36
^aThis work. ^bHarvey et. al.⁸⁷ ^cActive thermochemical Tables (ATcT).⁸⁶

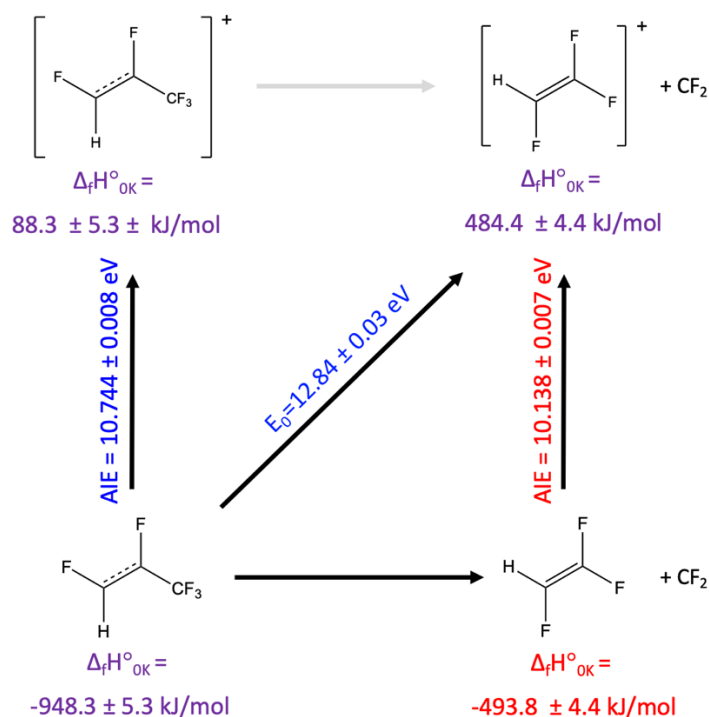


Figure 17. Thermochemical cycle of *cis*-1,2,3,3,3-pentafluoropropene (PFP) system and its corresponding CF₂-loss pathway. The ionization energy of PFP and the 0 K appearance energy of the fragment are experimentally derived and shown in blue while new thermochemical values determined in this work are shown in purple and literature values are shown in red. The 0 K heats of formations used in this cycle are shown in Table 4.

The *m/z* 82 dissociation channel corresponds to the formation of a trifluoroethylene cation (C₂HF₃⁺) [9b] and a CF₂ neutral from the molecular ion [1b]. Although this dissociation involves isomerization, the transition state is submerged, so the appearance energy corresponds to the thermochemical limit. The heat of formation of C₂HF₃⁺ can be derived based on available

literature. The AIE of C_2HF_3^+ is reported as 10.138 ± 0.007 eV⁸⁸ and the $\Delta_f H_{0\text{K}}(\text{C}_2\text{HF}_3) = -493.8 \pm 4.4$.⁸⁷ Therefore the $\Delta_f H_{0\text{K}}(\text{C}_2\text{HF}_3^+)$ is calculated as 484.4 ± 4.4 kJ/mol. The heat of formation of *cis*-1,2,3,3,3-trifluoropropene can be calculated since the heat of formations for both fragments are known and the appearance energy of the fragment ion is derived experimentally. With $E_0 = 12.84 \pm 0.03$, $\Delta_f H_{0\text{K}}(\text{C}_2\text{HF}_3^+) = 484.368 \pm 4.4$ kJ/mol, and $\Delta_f H_{0\text{K}}(\text{CF}_2) = -195.0 \pm 2.9$ kJ/mol⁸⁶, we determined the $\Delta_f H_{0\text{K}}(\text{PFP}) = -948.3 \pm 5.3$ kJ/mol. As the lowest energy m/z 113 (fluorine loss) dissociation channel involves a higher energy transition state (a reverse barrier), a heat of formation for C_3HF_4^+ was not determined.

Conclusions

We have studied the dissociative photoionization of 3,3,3-trifluoropropene (TFP) and *cis*-1,2,3,3,3-pentafluoropropene (PFP) using imaging PEPICO spectroscopy. The TFP adiabatic ionization energy was determined to be 11.17 ± 0.01 eV based on the threshold photoelectron spectrum and Franck–Condon simulations. Threshold photoionization time-of-flight mass spectra of TFP revealed four main fragment ions: m/z 95 (H-loss), 77 (F-loss), 46 (CF_2 -loss), and 27 (CF_3 -loss). Although there is a possibility for a direct hydrogen loss fragment ion, the most energetically favorable fragment ions are formed through isomerization of the molecular ion involving a fluorine shift. The lowest energy m/z 95 fragment ions are *cis* and *trans* allylic isomers of $\text{C}_3\text{H}_2\text{F}_3^+$, differing by only 0.04 eV. The next dissociation channel, F loss, can occur through homolytic bond breaking, also leading to an allylic fragment ion structure. The next dissociation channel is CF_2 loss, which (similarly to H loss) requires a rearrangement, made possible by the highly mobile fluorine atoms in the ion. The highest-energy dissociation channel in the studied energy range is CF_3 loss, taking place by bond rupture in the original molecular ion to form the non-classical vinyl cation. At high internal energies, numerous dissociation channels

become energetically allowed because of low-barrier isomerization processes. Because of the added complexity, the specific pathways contributing to the dissociation processes seen in the breakdown diagram cannot be identified experimentally. Through the CF_3 -loss dissociation channel, the heat of formation of the neutral TFP was determined to be -611.6 ± 8.4 kJ/mol, in good agreement with literature values. The heats of formation of two ions, $\text{CH}_2\text{CHCF}_2^+$ and CH_2CHF^+ , were also reported for the first time as 546 ± 10 kJ/mol and 846.6 ± 8.5 kJ/mol. We also confirmed a third heat of formation value, that of CHFCHCF_2^+ , previously measured by photoionization of *trans*-1,3,3,3-tetrafluoropropene. The heat of formation of $\text{C}_3\text{H}_2\text{F}_3^+$ is reported as 362.2 ± 8.5 kJ/mol.

From the TPES, experimental adiabatic ionization energy of *cis*-1,2,3,3,3-pentafluoropropene (PFP) was determined as 10.744 ± 0.008 eV. There are four parallel dissociative ionization channels for PFP leading to fragment ions at m/z 113 (F loss), 82 (CF_2 loss), 69 (C_2HF_2 loss), and 51 (C_2F_3 loss), with the notable absence of a hydrogen-loss channel. Although fluorine loss could also occur directly from the molecular ion, the lowest-energy pathway is shown to involve prior isomerization steps with fluorine and hydrogen shifts. At slightly higher energies, two new, closely related, fluorine-loss channels can also contribute. These dissociations can happen through a direct fluorine loss to create the *cis* [**7b**] fragment ion or from an isomerized molecular ion to create the *trans* [**8b**] fragment ion. The next dissociation channel observed in the breakdown diagram is CF_2 loss, which is necessarily preceded by a fluorine shift. The F-loss and CF_2 -loss processes were modeled with a statistical rate model to extract experimental 0 K appearance energies. High-energy processes, however, are very congested as numerous dissociation channels become energetically allowed and, at the same time, two minor channels also open up. According to theory, the lowest-energy C_2HF_2 -loss and

C_2F_3 -loss (yielding CF_3^+ and CHF_2^+ ions, respectively) pathways both involve fluorine and hydrogen rearrangements, but there are two other C_2HF_2 -loss direct dissociation channels 0.4 eV higher. The heat of formation of the m/z 82 trifluoroethylene cation [9b] (CHFCF_2) was calculated as 484.4 ± 4.4 kJ/mol from literature thermochemical values. With this, the heat of formation of the neutral PFP was determined for the first time as -948.3 ± 5.3 kJ/mol.

All three fluoropropenes, 3,3,3-trifluoropropene (TFP), *trans*-1,3,3,3-tetrafluoropropene,⁶⁹ and *cis*-1,2,3,3,3-pentafluoropropene (PFP), show similarities where several rearrangement processes occur in the internal energy selected molecular ions, made possible by the vagabond nature of the fluorine atoms. These isomerizations allow for the formation of H-loss and F-loss allylic structures, which are typically the most stable fragment ion candidates. In the two smaller HFOs ion, the dissociations that do occur follow the same order (with increasing internal energy), where H loss is first, followed by F loss, and then CF_2 loss. However, PFP ions do not exhibit a hydrogen-loss dissociation, as fluorine loss is lower in energy. At higher energies, TFP also shows a CF_3 -loss dissociation and PFP also show C_2HF_2 and C_2F_3 losses but, according to our calculations, several new rearrangement pathways open up, representing new ways for fluorine-loss dissociation.

Acknowledgements

This work was supported by the National Science Foundation under CHE1665464. The experiments were carried out at the VUV beamline of the Swiss Light Source of the Paul Scherrer Institute with support from the Swiss Federal Office for Energy (BFE Contract No. SI/501269-01).

REFERENCES

1. Ray, A. W.; Weidner, P.; Bodi, A.; Sztáray, B. The Vagabond Fluorine Atom: Dissociative Photoionization of trans- 1,3,3,3-Tetrafluoropropene. *ACS Publications* **2020**.
2. Tomassetti, S.; Nicola, G. D.; Kondou, C. Triple point measurements for new low- global-warming-potential refrigerants: hydro-fluoro-olefins, hydro-chloro-fluoro-olefins, and trifluoroiodomethane. *Int. J. Refrig.* **2021**.
3. Yang, L.; da Rocha, Sandro R. P. Understanding Solvation in the Low Global Warming Hydrofluoroolefin HFO-1234ze Propellant. *J Phys Chem B* **2014**, *118*, 10675-10687.
4. Sztáray, B.; Voronova, K.; Torma, K. G.; Covert, K. J.; Bodi, A.; Hemberger, P.; Gerber, T.; Osborn, D. L. CRF-PEPICO: Double velocity map imaging photoelectron photoion coincidence spectroscopy for reaction kinetics studies. *J. Chem. Phys.* **2017**, *147*, 013944.
5. Johnson, M.; Bodi, A.; Schulz, L.; Gerber, T. Vacuum ultraviolet beamline at the Swiss Light Source for chemical dynamics studies. *Nuclear Instruments & Methods in Physics Research Section A-accelerators Spectrometers Detectors and Associated Equipment - NUCL INSTRUM METH PHYS RES A* **2009**, *610*, 597-603.
6. Brehm, B.; von Puttkamer, E. Koinzidenzmessung von Photoionen und Photoelektronen bei Methan. *Zeitschrift für Naturforschung A* **1967**, *22*, 8-10.
7. Weidner, P.; Voronova, K.; Bodi, A.; Sztáray, B. Dissociative photoionization of 1,3-dioxolane: We need six channels to fit the elephant. *J. Mass Spectrom.* **2020**, *55*, e4522.
8. Baer, T.; Sztáray, B.; Kercher, J. P.; Lago, A. F.; Bödi, A.; Skull, C.; Palathinkal, D. Threshold photoelectron photoion coincidence studies of parallel and sequential dissociation reactions. *Phys. Chem. Chem. Phys.* **2005**, *7*, 1507-1513.
9. Shuman, N. S.; Ochieng, M. A.; Sztáray, B.; Baer, T. TPEPICO Spectroscopy of Vinyl Chloride and Vinyl Iodide: Neutral and Ionic Heats of Formation and Bond Energies. *The journal of physical chemistry. A, Molecules, spectroscopy, kinetics, environment, & general theory* **2008**, *112*, 5647-5652.
10. Wille, K. Synchrotron radiation sources. *Reports on Progress in Physics* **1991**, *54*, 1005-1067.
11. Winick, H.; Brown, G.; Halbach, K.; Harris, J. Wiggler and undulator magnets. *Phys Today* **1981**, *34*, 50-63.

12. Ng, C. *Vacuum Ultraviolet Photoionization and Photodissociation of Molecules and Clusters*; WORLD SCIENTIFIC: 1991; , pp 580.
13. Baer, T. Ion dissociation dynamics and thermochemistry by photoelectron photoion coincidence (PEPICO) spectroscopy. *International Journal of Mass Spectrometry; Volume 200: The state of the field as we move into a new millenium* **2000**, 200, 443-457.
14. Sztáray, B.; Bodi, A.; Baer, T. Modeling unimolecular reactions in photoelectron photoion coincidence experiments . *Journal of Mass Spectrometry* **2010**, 1233-1245.
15. Stockbauer, R. A threshold photoelectron—photoion coincidence mass spectrometer for measuring ion kinetic energy release on fragmentation. *International Journal of Mass Spectrometry and Ion Physics* **1977**, 25, 89-101.
16. Leyh, B. Ion Dissociation Kinetics in Mass Spectrometry☆. In *Encyclopedia of Spectroscopy and Spectrometry (Third Edition)*; Lindon, J. C., Tranter, G. E. and Koppenaal, D. W., Eds.; Academic Press: Oxford, 2017; pp 300-308.
17. Sztáray, B.; Baer, T. Suppression of hot electrons in threshold photoelectron photoion coincidence spectroscopy using velocity focusing optics. *Rev. Sci. Instrum.* **2003**, 74, 3763-3768.
18. Baer, T.; Li, Y. Threshold photoelectron spectroscopy with velocity focusing: An ideal match for coincidence studies. *International Journal of Mass Spectrometry - INT J MASS SPECTROM* **2002**, 219, 381-389.
19. Bodi, A.; Daniel Brannock, M.; Sztáray, B.; Baer, T. Tunneling in H loss from energy selected ethanol ions. *Phys. Chem. Chem. Phys.* **2012**, 14, 16047-16054.
20. Lang, M.; Holzmeier, F.; Hemberger, P.; Fischer, I. Threshold photoelectron spectra of combustion relevant isomers. *The journal of physical chemistry. A, Molecules, spectroscopy, kinetics, environment, & general theory* **2015**, 119, 3995.
21. Baer, T.; Tuckett, R. P. Advances in threshold photoelectron spectroscopy (TPES) and threshold photoelectron photoion coincidence (TPEPICO). *Phys. Chem. Chem. Phys.* **2017**, 19, 9698-9723.
22. Bodi, A.; Johnson, M.; Gerber, T.; Gengeliczki, Z.; Sztáray, B.; Baer, T. Imaging photoelectron photoion coincidence spectroscopy with velocity focusing electron optics. *Rev. Sci. Instrum.* **2009**, 80, 034101.
23. Eppink, André T. J. B.; Parker, D. H. Velocity map imaging of ions and electrons using electrostatic lenses: Application in photoelectron and photofragment ion imaging of molecular oxygen. *Rev. Sci. Instrum.* **1997**, 68, 3477-3484.

24. Chandler, D. W.; Houston, P. L. Two-dimensional imaging of state-selected photodissociation products detected by multiphoton ionization. *J. Chem. Phys.* **1987**, *87*, 1445-1447.
25. Chandezon, F.; Huber, B.; Ristori, C. A new-regime Wiley–McLaren time-of-flight mass spectrometer. *Rev. Sci. Instrum.* **1994**, *65*, 3344-3353.
26. Wiley, W. C.; McLaren, I. H. Time-of-Flight Mass Spectrometer with Improved Resolution. *Rev. Sci. Instrum.* **1955**, *26*, 1150-1157.
27. Davies, J. A.; LeClaire, J. E.; Continetti, R. E.; Hayden, C. C. Femtosecond time-resolved photoelectron–photoion coincidence imaging studies of dissociation dynamics. *J. Chem. Phys.* **1999**, *111*, 1-4.
28. Osborn, D. L.; Hayden, C. C.; Hemberger, P.; Bodi, A.; Voronova, K.; Sztáray, B. Breaking through the false coincidence barrier in electron–ion coincidence experiments. *J. Chem. Phys.* **2016**, *145*, 164202.
29. Baer, T.; Bodi, A.; Sztáray, B. Photoelectron–Photoion Coincidence Methods in Mass Spectrometry, (PEPICO)☆. In *Encyclopedia of Spectroscopy and Spectrometry (Third Edition)*; Lindon, J. C., Tranter, G. E. and Koppenaal, D. W., Eds.; Academic Press: Oxford, 2017; pp 635-649.
30. Bodi, A.; Sztáray, B.; Baer, T. Dissociative photoionization of mono-, di- and trimethylamine studied by a combined threshold photoelectron photoion coincidence spectroscopy and computational approach. *Phys. Chem. Chem. Phys.* **2006**, *8*, 613-623.
31. Bodi, A.; Sztáray, B.; Baer, T.; Johnson, M.; Gerber, T. Data acquisition schemes for continuous two-particle time-of-flight coincidence experiments. *Review of Scientific Instruments* **2007**.
32. Ferrier, B.; Boulanger, A.; Holland, D. M. P.; Shaw, D. A.; Mayer, P. M. Nitro–Nitrite Isomerization and Transition State Switching in the Dissociation of Ionized Nitromethane: A Threshold Photoelectron–Photoion Coincidence Spectroscopy Study. *Eur J Mass Spectrom (Chichester)* **2009**, *15*, 157-166.
33. Ackermann, T. Book Review: Thermochemical Kinetics. Methods for the Estimation of Thermochemical Data and Rate Parameters. By S. W. Benson. *Angew. Chem. Int. Ed Engl.* **1977**, *16*, 883.
34. Lifshitz, C. Time-resolved appearance energies, breakdown graphs, and mass spectra: The elusive “kinetic shift”. *Mass Spectrom. Rev.* **1982**, *1*, 309-348.
35. Chupka, W. A. Effect of Unimolecular Decay Kinetics on the Interpretation of Appearance Potentials. *J. Chem. Phys.* **1959**, *30*, 191-211.

36. Stevens, W.; Sztáray, B.; Shuman, N.; Baer, T.; Troe, J. Specific rate constants $k(E)$ of the dissociation of the halobenzene ions: analysis by statistical unimolecular rate theories. *J Phys Chem A* **2009**, *113*, 573-582.
37. Torma, K. G.; Voronova, K.; Sztáray, B.; Bodi, A. Dissociative Photoionization of the C₇H₈ Isomers Cycloheptatriene and Toluene: Looking at Two Sides of the Same Coin Simultaneously. *J Phys Chem A* **2019**, *123*, 3454-3463.
38. Lifshitz, C. Kinetic Shifts. *Eur J Mass Spectrom (Chichester)* **2002**, *8*, 85-98.
39. Stevens, W.; Sztáray, B.; Shuman, N.; Baer, T.; Troe, J. Specific Rate Constants $k(E)$ of the Dissociation of the Halobenzene Ions: Analysis by Statistical Unimolecular Rate Theories. *J Phys Chem A* **2009**, *113*, 573-582.
40. Hinde, R. J. Reaction Kinetics (Pilling, Michael J.; Seakins, Paul W.). *J. Chem. Educ.* **1997**, *74*, 625.
41. Klippenstein, S. J. Variational optimizations in the Rice–Ramsperger–Kassel–Marcus theory calculations for unimolecular dissociations with no reverse barrier. *J. Chem. Phys.* **1992**, *96*, 367-371.
42. Baer, T.; Mayer, P. M. Statistical Rice-Ramsperger-Kassel-Marcus quasiequilibrium theory calculations in mass spectrometry. *J. Am. Soc. Mass Spectrom.* **1997**, *8*, 103-115.
43. Marcus, R. A.; Rice, O. K. The Kinetics of the Recombination of Methyl Radicals and Iodine Atoms. *J. Phys. Chem.* **1951**, *55*, 894-908.
44. Rice, O. K.; Ramsperger, H. C. THEORIES OF UNIMOLECULAR GAS REACTIONS AT LOW PRESSURES. II. *J. Am. Chem. Soc.* **1928**, *50*, 617-620.
45. Rice, O. K.; Ramsperger, H. C. THEORIES OF UNIMOLECULAR GAS REACTIONS AT LOW PRESSURES. *J. Am. Chem. Soc.* **1927**, *49*, 1617-1629.
46. Kassel, L. S. Studies in Homogeneous Gas Reactions. I. *J. Phys. Chem.* **1928**, *32*, 225-242.
47. Hinshelwood, C. N.; Sidgwick, N. V. On the theory of unimolecular reactions. *Proceedings of the Royal Society of London. Series A, Containing Papers of a Mathematical and Physical Character* **1926**, *113*, 230-233.
48. Rosenstock, H. M.; Wallenstein, M. B.; Wahrhaftig, A. L.; Eyring, H. Absolute Rate Theory for Isolated Systems and the Mass Spectra of Polyatomic Molecules. *Proc. Natl. Acad. Sci. U. S. A.* **1952**, *38*, 667-678.

49. Baer, T.; Hase, W. L. *Unimolecular Reaction Dynamics: Theory and Experiments*; Oxford University Press: New York, 1996; , pp 446.
50. Sztáray, B.; Baer, T. Consecutive and Parallel Dissociation of Energy-Selected $\text{Co}(\text{CO})_3\text{NO}^+$ Ions. *J Phys Chem A* **2002**, *106*, 8046-8053.
51. Frisch, M. J.; Trucks, G. W.; Schlegel, H. B.; Scuseria, G. E.; Robb, M. A.; Cheeseman, J. R.; Scalmani, G.; Barone, V.; Mennucci, B.; Petersson, G. A. Gaussian 09. **2009**.
52. Vignale, G.; Rasolt, M. Density-functional theory in strong magnetic fields. *Phys. Rev. Lett.* **1987**, *59*, 2360-2363.
53. Levy, M. Universal variational functionals of electron densities, first-order density matrices, and natural spin-orbitals and solution of the ν -representability problem. *Proc. Natl. Acad. Sci. USA* **1979**, *76*, 6062.
54. Becke, A. D. Density-functional thermochemistry. III. The role of exact exchange. *J. Chem. Phys.* **1993**, *98*, 5648-5652.
55. Lee, C.; Yang, W.; Parr, R. G. Development of the Colle-Salvetti correlation-energy formula into a functional of the electron density. *Phys. Rev. B* **1988**, *37*, 785-789.
56. Becke, A. D. Density-functional exchange-energy approximation with correct asymptotic behavior. *Phys. Rev. A* **1988**, *38*, 3098-3100.
57. Becke, A. D. A new mixing of Hartree-Fock and local density-functional theories. *J. Chem. Phys.* **1993**, *98*, 1372-1377.
58. Lee, C.; Yang, W.; Parr, R. G. Development of the Colle-Salvetti correlation-energy formula into a functional of the electron density. *Phys. Rev. B. Condens Matter* **1988**, *37*, 785-789.
59. Peng, C.; Ayala, P. Y.; Schlegel, H. B.; Frisch, M. J. Using redundant internal coordinates to optimize equilibrium geometries and transition states. *J. Comput. Chem.* **1996**, *17*, 49-56.
60. Peng, C.; Bernhard Schlegel, H. Combining Synchronous Transit and Quasi-Newton Methods to Find Transition States. *Isr. J. Chem.* **1993**, *33*, 449-454.
61. Fukui, K. The path of chemical reactions - the IRC approach. *Acc. Chem. Res.* **1981**, *14*, 363-368.
62. Curtiss, L. A.; Redfern, P. C.; Raghavachari, K. Gaussian-4 theory. *J. Chem. Phys.* **2007**, *126*, 084108.

63. Kirsch, P. Halofluorocarbons, Hydrofluorocarbons, and Related Compounds. In *Modern Fluoroorganic Chemistry* John Wiley & Sons, Inc.: 2013; pp 245-298.
64. Papadimitriou, V. C.; Lazarou, Y. G.; Talukdar, R. K.; Burkholder, J. B. Atmospheric Chemistry of $\text{CF}_3\text{CF}=\text{CH}_2$ and (Z)- $\text{CF}_3\text{CF}=\text{CHF}$: Cl and NO_3 Rate Coefficients, Cl Reaction Product Yields, and Thermochemical Calculations. *J Phys Chem A* **2011**, *115*, 167-181.
65. Tovar, C. M.; Blanco, M. ' . B.; Barnes, I. D.; Wiesen, P.; Teruel, M. A. Gas-phase reactivity study of a series of hydrofluoroolefins (HFOs) toward OH radicals and Cl atoms at atmospheric pressure and 298 K. *Atmos. Environ.* **2014**, *88*, 107-114.
66. Takhistov, V. V.; Ponomarev, D. A. Isodesmic reactions and thermochemistry of ions. *Org. Mass Spectrom.* **1994**, *29*, 395-412.
67. Steele, W. C.; Stone, F. C. A. An Electron Impact Study of 1,1,1-Trifluoroethane, 1,1,1-Trifluoropropane and 3,3,3-Trifluoropropene. *J. Am. Chem. Soc.* **1962**, *84*, 3450-3454.
68. Bralsford, R.; Harris, P. V.; Price, W. C. The effect of fluorine on the electronic spectra and ionization potentials of molecules. *Proceedings of the Royal Society of London. Series A. Mathematical and Physical Sciences* **1960**, *258*, 459-469.
69. Ray, A. W.; Weidner, P.; Bodi, A.; Sztáray, B. The Vagabond Fluorine Atom: Dissociative Photoionization of trans-1,3,3,3-Tetrafluoropropene. *J Phys Chem A* **2020**, *124*, 3738-3746.
70. Cox, J. D.; Pilcher, G. Thermochemistry of Organic and Organometallic Compounds. Academic Press, London and New York 1970. 643 Seiten. Preis: 170s. *Berichte der Bunsengesellschaft für physikalische Chemie* **1970**, *74*, 727.
71. Paulechka, E.; Kazakov, A. Critical Evaluation of the Enthalpies of Formation for Fluorinated Compounds Using Experimental Data and High-Level Ab Initio Calculations. *J. Chem. Eng. Data* **2019**, *64*, 4863-4874.
72. Lifshitz, C.; Long, F. A. Appearance Potentials and Mass Spectra of C_3F_6 , $\text{C}_3\text{F}_5\text{Cl}$, and c- C_3F_6 . *J. Phys. Chem.* **1965**, *69*, 3741-3746.
73. Berman, D. W.; Bomse, D. S.; Beauchamp, J. L. Photoionization threshold measurements for CF_2 loss from perfluoropropylene, perfluorocyclopropane, and trifluoromethylbenzene. The heat of formation of CF_2 and consideration of the potential-energy surface for interconversion of isomeric C_3F_6 neutrals and ions. *International Journal of Mass Spectrometry and Ion Physics* **1981**, *39*, 263-271.
74. Jarvis, G. K.; Boyle, K. J.; Mayhew, C. A.; Tuckett, R. P. Threshold Photoelectron–Photoion Coincidence Spectroscopy of Perfluorocarbons. 2. Unsaturated

- and Cyclic Perfluorocarbons C₂F₄, C₃F₆, 2-C₄F₈, and c-C₄F₈. *J Phys Chem A* **1998**, *102*, 3230-3237.
75. Bodi, A.; Johnson, M.; Gerber, T.; Gengeliczki, Z.; Sztáray, B.; Baer, T. T. Imaging Photoelectron photoion coincidence spectroscopy with velocity focusing electron optics. *Review of Scientific Instruments* **2009**.
 76. Torma, K. G.; Voronova, K.; Sztáray, B.; Bodi, A. Dissociative Photoionization of the C₇H₈ Isomers Cycloheptatriene and Toluene: Looking at Two Sides of the Same Coin Simultaneously. *J Phys Chem A* **2019**, *123*, 3454-3463.
 77. Voronova, K.; Mozaffari Easter, C. M.; Covert, K. J.; Bodi, A.; Hemberger, P.; Sztáray, B. Dissociative Photoionization of Diethyl Ether. *J Phys Chem A* **2015**, *119*, 10654-10663.
 78. Peng, C.; Bernhard Schlegel, H. Combining Synchronous Transit and Quasi-Newton Methods to Find Transition States. *Isr. J. Chem.* **1993**, *33*, 449-454.
 79. Chunyang, P.; Ayala, P. Y.; Schlegel, H. B. Using Redundant Internal Coordinates to Optimize Equilibrium Geometries and Transition States. *Journal of Computational Chemistry* **1996**, *17*, No. 1, 49-56.
 80. Curtiss, L. A.; Redfern, P. C.; Raghavachari, K. Gaussian-4 theory. *J. Chem. Phys.* **2007**, *126*, 084108.
 81. Baer, T.; Hase, W. L. Unimolecular reaction dynamics: theory and experiments. **1996**, 438.
 82. McKay, J. Algorithm 262: Number of restricted partitions of N. *Communications of the ACM* **1965**, *8*, 493.
 83. Pople, J. A. The structure of the vinyl cation. *Chemical physics letters* **1987**, *137*, 10-12.
 84. Wu, X.; Zhou, X.; Hemberger, P.; Bodi, A. The ionization energy of the vinyl radical: a Mexican standoff with a happy ending. *Phys. Chem. Chem. Phys.* **2019**, *21*, 22238-22247.
 85. Kolesov, V. P.; Marynov, A. M.; Skuratov, S. M. Standard Enthalpy. of Formation of 1,1,1-Trifluoropropen. **1967**, 482-484.
 86. Ruscic, B.; Bross, D. H. Active Thermochemical Tables (ATcT) Version 1.122r. <https://atct.anl.gov/> (accessed November 19, 2021).
 87. Harvey, J.; Bodi, A.; Tuckett, R. P.; Sztáray, B. Dissociation dynamics of fluorinated ethene cations: from time bombs on a molecular level to double-regime dissociators. *Phys. Chem. Chem. Phys.* **2012**, *14*, 3935-3948.

88. Harvey, J.; Hemberger, P.; Bodi, A.; Tuckett, R. P. Vibrational and electronic excitations in fluorinated ethene cations from the ground up. *J. Chem. Phys.* **2013**, *138*, 124301.